The Astrophysical Journal, 982:29 (23pp), 2025 March 20 https://doi.org/10.3847/1538-4357/ad96ad

The Response of Planetary Atmospheres to the Impact of Icy Comets. I. Tidally Locked Exo-Earths

F. Sainsbury-Martinez[1], C. Walsh[1], and G. Cooke[1,2]
[1] School of Physics and Astronomy, University of Leeds, Leeds LS2 9JT, UK
[2] Institute of Astronomy, University of Cambridge, UK

Received 2024 September 18; revised 2024 November 11; accepted 2024 November 24; published 2025 March 12

Abstract

Impacts by rocky and icy bodies are thought to have played a key role in shaping the composition of solar system objects, including the Earth's habitability. Hence, it is likely that they play a similar role in exoplanetary systems. We investigate how an icy cometary impact affects the atmospheric chemistry, climate, and composition of an Earth-like, tidally locked, terrestrial exoplanet, a prime target in the search for a habitable exoplanet beyond our solar system. We couple a cometary impact model, which includes thermal ablation and pressure driven breakup, with the 3D Earth system model WACCM6/CESM2 and use this model to investigate the effects of the water and thermal energy delivery associated with an $R = 2.5$ km pure water ice cometary impact on an Earth-like atmosphere. We find that water is the primary driver of longer timescale changes to the atmospheric chemistry and composition by acting as a source of opacity, cloud ice, and atmospheric hydrogen/oxygen. The water opacity drives heating at $\sim 5 \times 10^{-4}$ bar and cooling below, due to a decreased flux reaching the surface. The increase in atmospheric hydrogen and oxygen also drives an increase in the abundance of hydrogen/oxygen-rich molecules, with the exception of ozone, whose column density decreases by ~10%. These atmospheric changes are potentially observable for ~1–2 yr postimpact, particularly those associated with cloud ice scattering. They also persist, albeit at a much reduced level, to our quasi–steady state, suggesting that sustained bombardment or multiple large impacts have the potential to shape the composition and habitability of terrestrial exoplanets.

Unified Astronomy Thesaurus concepts: Exoplanet atmospheres (487); Atmospheric composition (2120); Atmospheric dynamics (2300); Computational astronomy (293)

1. Introduction

Material delivery associated with icy and rocky body impacts is proposed to have played a significant role in shaping the composition and the habitability of solar system planets. For example, material delivery by cometary and asteroidal impacts has been invoked in an effort to explain (i) Jupiter's supersolar metallicity, both for models that consider a more general enrichment (T. Guillot et al. 2004; J. J. Fortney & N. Nettelmann 2010) and for models in which the outer atmosphere alone is enriched (S. Müller & R. Helled 2024), (ii) the dawn–dusk asymmetry of Mercury's exosphere (W. Benz et al. 1988; P. Pokorný et al. 2017), and (iii) the atmospheres of Mars (J. M. Y. Woo et al. 2019) and Venus (M. Y. Marov & S. I. Ipatov 2018, 2023).

Cometary and asteroidal impacts have also been invoked as a key mechanism by which the early Earth's composition and atmosphere was shaped, potentially playing a critical role in the delivery of materials, such as complex organic molecules (P. Ehrenfreund et al. 2002) or water, which are key to setting the Earth's habitability (A. H. Delsemme 2000; G. R. Osinski et al. 2020). For example, analysis of numerical models of the migration of small bodies from the outer solar system inward toward the terrestrial planets suggests that the total mass of water delivered from the feeding zone of the giant planets ($\sim 2 \times 10^{-4} M_{\oplus}$) to Earth is on the order of the mass of the Earth's oceans (S. I. Ipatov & J. C. Mather 2003, 2004; D. P. O'Brien et al. 2014; M. Y. Marov & S. I. Ipatov 2023), with similar relative water mass fractions also being delivered to Venus and Mars. Even the migration of dust from collisions of minor bodies throughout the solar system could play a significant role in delivering volatilities and organic molecules to the terrestrial planets (M. Y. Marov & S. I. Ipatov 2005).

Under the assumption that exoplanetary systems form in a similar manner to our own solar system, we can infer that planetary bombardment and cometary/asteroidal impacts should also have played a significant role in shaping the composition, atmosphere, and hence habitability of exoplanets. For example, R. J. Anslow et al. (2023) explore the ability of cometary impacts to deliver prebiotic molecules to rocky/terrestrial exoplanets, suggesting that prebiotic molecules are more likely to survive impacts with low-mass planets orbiting high-mass stars due to the lower impact velocity of such a system. In a similar vein, K. Frantseva et al. (2020) suggest that volatile delivery from exoplanetary system belts may have played a significant role in delivering volatiles to terrestrial planets that formed within the water snowline (i.e., within a region of the protoplanetary disk that was too hot for water to condense and form ice), potentially delivering enough material to account for an Earth-like atmospheric mass. A. C. Childs et al. (2022) confirm that such an impact driving belt might exist around an M dwarf star, albeit with a lower occurrence rate than in higher-mass systems. Finally, F. Sainsbury-Martinez & C. Walsh (2024) discussed the role that icy cometary impacts might have in setting the observed low C/O ratios and high metallicities of hot gas giants.

This is particularly true for terrestrial planets orbiting cooler stars, such as low-mass M dwarfs. The lower luminosities of these host stars result in the habitable zone—which is generally defined as the region around a star in which the equilibrium temperature of a planet would fall into the range that allows for liquid surface water without inducing a runaway greenhouse effect (R. K. Kopparapu et al. 2013; G. Valle et al. 2014)—lying significantly closer to the host star than it would for a Sun-like star. An example is the TRAPPIST-1 system, where the habitable zone around this cool M8 red-dwarf host star lies between ∼0.025 and ∼0.05 au, which corresponds to to an orbital period of between ∼4.5 and ∼13.5 days (M. Gillon et al. 2013, 2016). In turn, this leads to an increase in the orbital velocity of habitable-zone planets: the orbital velocity of TRAPPIST-1e is ∼1.6 times that of the Earth. This increase in orbital velocity, when combined with the effects of gravitational focusing by the nearby host star (D. Nesvorný et al. 2023), suggests that impact rates for habitable-zone planets orbiting M dwarfs have the potential to be significantly higher than that experienced by the Earth, although this may be somewhat tempered by the lower protoplanetary disk masses associated with low-mass stars (Y. Alibert & W. Benz 2017). Note that the multiplanet nature of the TRAPPIST-1 system may also lead to an enhanced impact rate. For example, J. L. Smallwood et al. (2018) discuss the role that multiplanet resonances can have in increasing the planetesimal flux.

In addition to its possible effect on the cometary impact rate, orbiting so close to a potentially active M dwarf also may also have significant implications for the atmospheric chemistry and dynamics, effects that are likely to influence the response of a terrestrial planet's atmosphere to an icy cometary impact.

To start, the small orbital distance between such habitable-zone terrestrial planets and their hosts stars will lead to significant angular momentum exchange, via tidal torques, between the two bodies. This will result in the synchronization of the planetary rotation rate and orbital period, leaving us with a tidally locked planet with a permanently illuminated dayside and permanently dark, and hence cooler, nightside (S. H. Dole 1964; R. Barnes 2017). In turn, this day–night insolation contrast leads to the formation of strong horizontal pressure and temperature gradients that, in concert with the somewhat rapid planetary rotation, shape and drive the global atmospheric circulations. For example, the strong day–night pressure/temperature gradient can lead to the formation of a global overturning circulation in which air parcels rise on the dayside, are advected toward the nightside in the stratosphere and above, and then sink surfaceward with near-surface night-to-day winds completing the circulation (A. P. Showman et al. 2013). Simultaneously, the strong off-equator Coriolis effect can lead to the formation of standing Rossby and Kelvin waves that pump eastward angular momentum from high latitudes to low, potentially driving to the formation of (a) superrotating jet (s) (A. P. Showman & L. M. Polvani 2011). Together, these circulations have the potential to significantly alter the overall climate of the planet (L. Carone et al. 2015), including the atmospheric chemistry and composition. A good example of this is atmospheric ozone, the formation and destruction of which is sensitive to UV insolation rates. Consequently, multiple studies have shown that day–night advection can lead to the enrichment of the atmospheric ozone on the nightside and/or at the poles (e.g., E. Proedrou & K. Hocke 2016; H. Chen et al. 2018; J. S. Yates et al. 2020; M. Braam et al. 2023; A. Bhongade et al. 2024; G. J. Cooke et al. 2024).

In addition to its implications for the orbital dynamics and atmospheric circulations, orbiting a cooler M dwarf can also affect the atmospheric chemistry more directly due to differences in the stellar spectrum. Specifically, differences in the UV spectrum can drive significant changes in the atmospheric chemistry due to the sensitivity of many photochemical reactions, such as the formation of ozone or the photodissociation of water, to both the strength and shape (wavelength) of the incoming UV irradiation (see, for example, J. L. Grenfell et al. 2014; V. S. Meadows et al. 2018; T. Kozakis et al. 2022).

The importance of these effects emphasizes the need to study the affects of cometary impacts on atmospheric dynamics and chemistry in a 3D and time-dependent manner. Here we conduct a pilot study, investigating a well-documented parameter regime (a tidally locked exo-Earth atmosphere) with a robust atmospheric model, laying the foundations for future studies that consider atmospheres more reminiscent of young terrestrial planets. Impact rates are expected to be much higher for young planets, such as the Archean Earth (e.g., W. F. Bottke & M. D. Norman 2017; R. Brasser et al. 2020), and they likely played a significant role in delivering volatiles, such as oxygen or water (e.g., C. F. Chyba et al. 1990; Z. R. Todd & K. I. Öberg 2020; J. P. Itcovitz et al. 2022).

To study such the effects of a single, icy, cometary impact, we couple the cometary ablation and breakup model of F. Sainsbury-Martinez & C. Walsh (2024) with the Whole Atmosphere Community Climate Model (WACCM6) Coupled Earth System Model (CESM2), an Earth system model that has been used to explore the atmospheric dynamics and chemistry of both Earth-analog (G. J. Cooke et al. 2022; B. Liu et al. 2023) and tidally locked exoplanets (G. J. Cooke et al. 2023, 2024). Then, as discussed in Section 2, we use this coupled cometary impact/climate model to study how the impact of a single pure water ice comet affects the atmosphere of a tidally locked Earth-analog exoplanet. Specifically, we consider an impact with TRAPPIST-1e, which is the TRAPPIST planet with the highest likelihood of hosting a terrestrial, and hence potentially habitable, atmosphere (E. T. Wolf 2017).

An icy cometary impact affects the atmosphere of a tidally locked exoplanet in two ways. First it acts as a source of mass/water delivery, and second it delivers thermal energy to the atmosphere as the kinetic energy of the impacting comet is reduced. We discuss the combined effects of these two components of the cometary impact on our tidally locked Earth-like atmosphere in Section 3. We also ran two additional models in which we isolate the two components of the cometary impact–driven delivery. A discussion of these models, and the differences in both the strength and the timescale of the atmospheric response to isolated mass/water deposition (Appendix A.1) and heat deposition (Appendix A.2), can be found in the Appendix. We finish, in Section 4, with some concluding remarks, discussing the implications of our results for our understanding of the compositions of terrestrial exoplanetary atmospheres as well as possible directions that this work will take in the future.

2. Method

To understand how an icy cometary impact affects the atmosphere of a terrestrial, tidally locked exoplanet, we couple a slightly modified version of the parameterized cometary impact model of F. Sainsbury-Martinez & C. Walsh (2024; Section 2.1) with a version of the Earth system model WACCM6/CESM2, which has been modified to allow for synchronous rotation[3] and the delivery of both thermal energy and water due to a cometary impact[4] (Section 2.2). This coupled model is then used to study the impact of a pure water ice comet, with a radius of 2.5 km and a density of 1 g cm^{-3}, with the atmosphere of a quasi-steady-state TRAPPIST-1e model with preindustrial atmospheric composition and an Earth-like land–ocean distribution, including orography (mountains) and a dynamic ocean. We use this configuration because it has been robustly tested and benchmarked (G. J. Cooke et al. 2022, 2023, 2024; B. Liu et al. 2023; A. Bhongade et al. 2024; F. Sainsbury-Martinez et al. 2024).

2.1. Cometary Impact Model

To model our icy cometary impacts, we adopt the parameterized cometary ablation and breakup model of F. Sainsbury-Martinez & C. Walsh (2024), albeit with a modification to the thermal energy deposition during the ablation phase to address the lower heat capacity of the outer atmosphere of a terrestrial planet when compared with a hot gas giant.

This model assumes that the comet encounters the atmosphere with a zero angle of incidence (i.e., $\cos(\theta) = 1$), that it remains spherical until breakup (i.e., no deformation), and that its interaction with the atmosphere can be split into two distinct phases: in the outer atmosphere, where the pressure/atmospheric density is low, the comet slows due to atmospheric drag, which drives surface ablation (phase 1). However as the density of the atmosphere increases, so too does the drag and stress on the comet, leading to an increase in the ram pressure and eventual cometary breakup (phase 2), when the ram pressure exceeds the tensile strength of the cometary ice (Q. R. Passey & H. J. Melosh 1980; C. Mordasini et al. 2016). Note that a number of other complex physical phenomenon are hypothesized to play a key role in cometary breakup, such as deformation (i.e., pancaking—M.-M. Mac Low & K. Zahnle 1994; G. B. Field & A. Ferrara 1995) or surface instabilities (e.g., Rayleigh–Taylor—Y. Alibert et al. 2005b—or Kelvin–Helmholtz—D. G. Korycansky et al. 2002); however, as discussed in F. Sainsbury-Martinez & C. Walsh (2024), a careful consideration of ram-driven breakup alone is sufficient to reproduce the breakup locations of observed cometary impacts, such as Shoemaker–Levy 9 on Jupiter.

During the ablation phase of the cometary impact we model the velocity (V) and location of the comet in a time-dependent manner via the velocity evolution equation of Q. R. Passey & H. J. Melosh (1980):

$$\frac{dV}{dt} = g - \frac{C_D \rho_a A V^2}{M}, \tag{1}$$

where

$$A = S_F \left(\frac{M}{\rho_c}\right)^{\frac{2}{3}} \tag{2}$$

is the effective cross-sectional area of the spherical comet, $g = 9.1454$ m s^{-2} is the gravitational acceleration associated with the planet TRAPPIST-1e (E. Agol et al. 2021), $C_D = 0.5$ is the drag coefficient (of a sphere), ρ_a is the atmospheric density (taken from the input CESM atmospheric model), $S_F = 1.3$ is the shape factor (of a sphere), dt is the time step (which must be short enough to capture the impact), and ρ, dV, and M are the density, change in velocity, and remaining mass of the comet, respectively. Here we assume that the density of the comet is the same as pure water ice ($\rho = 1$ g cm^{-3}), that the radius of the comet is 2.5 km (which falls on the lower end of known cometary radii—M. F. A'Hearn 2011, and that the initial velocity of the comet is $V = 10$ km s^{-1}, the latter of which is approximately the escape velocity of TRAPPIST-1e. Note that we limit ourselves to smaller cometary impacts ($R = 2.5$ km) due to computational instabilities that occur for higher-mass/energy deposition rates. Hence the quantification performed here on the climate response to the impact can be considered a lower threshold since one would expect impacts from larger, more massive comets to have a greater influence on the atmosphere.

This velocity is then used to calculate the ablation driven mass deposition, which is given by

$$\frac{dM}{dt} = -\frac{C_H \rho_a A V^2}{2Q}\left(\frac{V^2 - V_{cr}^2}{V^2}\right), \tag{3}$$

where $C_H = 0.5$ is the heat transfer coefficient (V. V. Svetsov et al. 1995; Y. Alibert et al. 2005a), $Q = 2.5 \times 10^{10}$ erg g^{-1} is the heat of ablation of the cometary ice (pure water; C. Mordasini et al. 2016), and $V_{cr} = 3$ km s^{-1} is the critical velocity below which no ablation occurs (Q. R. Passey & H. J. Melosh 1980).[5]

The thermal energy deposition in the outer atmosphere is given by

$$\frac{dE}{dt} = 0.5\pi V^3 \rho_a R^2. \tag{4}$$

Here, rather than directly depositing a fraction of the lost kinetic energy of the comet into the atmosphere, we instead consider a reduced thermal input based upon interactions between the comet and the column of atmospheric gas it passes through. More specifically, we calculate the deposited thermal energy by working out how many "static" molecules interact with the comet at each time step, with each molecule gaining kinetic energy based upon the instantaneous velocity of the comet, i.e., by assuming that the comet scatters molecules out of the column it passes through with a velocity equal to the cometary velocity. Even then, as we discuss in Section 2.2, the amount of thermal energy added to the atmosphere is at the limit of what our model can computationally handle.

At the same time, we also calculate the ram pressure ($P_{\rm ram}$) and compare this against the tensile strength of the comet ($\sigma_T = 4.6 \times 10^6$ erg cm^{-2}; the tensile strength of an icy planetesimal taken from C. Mordasini et al. 2016), with cometary breakup considered to have occurred when

$$P_{\rm ram} > \sigma_T, \text{ where} \tag{5}$$

$$P_{\rm ram} = C_D \rho_A V^2. \tag{6}$$

---

[3] http://github.com/exo-cesm/

[4] http://gitlab.com/leeds_work/cesm_comet/

[5] Note that this equation is incorrect in Q. R. Passey & H. J. Melosh (1980), as well as a number of other works that have cited this work. Specifically, their version of Equation (3) (Equation 2 in Q. R. Passey & H. J. Melosh 1980) is missing a factor of V (i.e. V^2 vs V^3) in the first term.

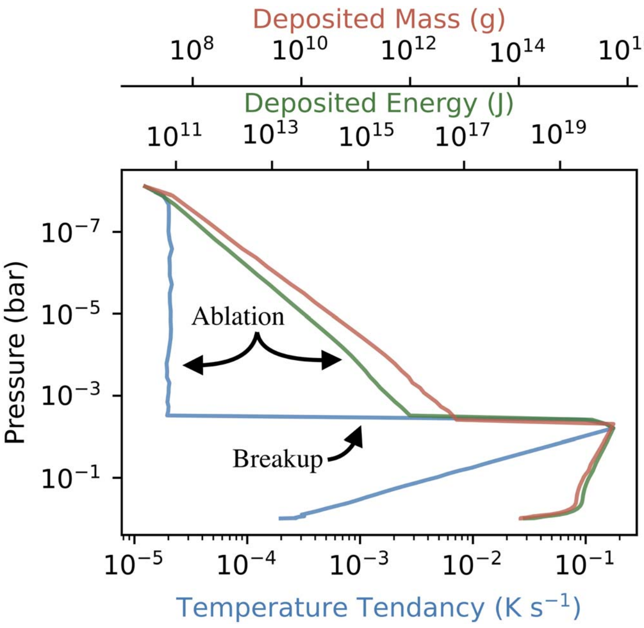

Figure 1. The initial vertical mass (red) and thermal energy distribution profile (green) generated by our cometary ablation and breakup model for a pure water ice comet, with a radius of 2.5 km and a density of 1 g cm^{-3}, impacting the substellar point of our TRAPPIST-1e-like atmospheric model. For computational reasons, this mass and energy are introduced to the model over a period of 10 days and with an initial horizontal spread of nine (3 × 3) columns. Further, due to the structure of WACCM6/CESM2's solver, the deposited energy must be converted into a local temperature tendency (i.e., rate of temperature change), which is then applied to each cell (blue).

Once this condition is fulfilled, the comet is destroyed and any remaining mass and kinetic energy is distributed deeper into the atmosphere over a pressure scale height. This is done using an exponentially decaying function, which is normalized to ensure that all cometary material/deposited energy is introduced to the atmosphere between the breakup site and the surface. This simulates the rapid breakup of cometary ice and the resulting mass/energy distribution due to the inertia of the impacting material without the need for complex fragment modeling.

The resulting mass and thermal energy deposition profiles for the impact of a pure water ice comet with the substellar point of TRAPPIST-1e are shown in Figure 1. A full list of the cometary parameters used to calculate these ablation profiles are given in Table 1. We discuss the background atmosphere with which these comets interact (i.e., which is used to calculate the profiles and to which the profiles are applied) below (Section 2.2).

Here we can see the two stages of our cometary impact. In the low-density outer atmosphere we find that both the mass (ablation) and thermal energy deposition rates increase with pressure and hence atmospheric density. However, there comes a point, around 4.8 x 10^{-3} bar (∼34 km above the surface) in our model, that the stresses on the comet have become too much, leading to breakup and the deposition of the majority of the comets ice and kinetic energy into the deeper atmosphere.

2.2. *Planetary Atmosphere Model*

In order to model the response of a tidally locked, terrestrial, exoplanetary atmosphere to an icy cometary impact, we couple the above ablation and breakup model to a TRAPPIST-1e-like atmospheric model calculated with the Earth system model WACCM6/CESM2. Additionally we also simulate an unimpacted reference case with which to compare our results and two additional coupled models, in which we explore the isolated effects of water/mass and thermal energy deposition and that are used to investigate the strength and lifetime of the changes associated with each component of the cometary impact.

Table 1
Parameters of the Impacting Icy Comet Considered in This Work

Parameter	Value	Unit
Radius R	2.5	km
Density ρ_c	1	g cm^{-3}
Initial Velocity V	10	km s^{-1}
Heat Transfer Coefficient C_H	0.5	⋯
Drag Coefficient C_D	0.5	⋯
Latent Heat of Ablation Q	2.5×10^{10}	erg g^{-1}
Tensile Strength σ_T	4×10^6	erg cm^{-2}

2.2.1. *WACCM6/CESM2*

WACCM6 is a well-documented (A. Gettelman et al. 2019), high-top (the atmosphere extends to 140 km—∼10^{-8} bar—above the surface) configuration of the open-source CESM2. It includes a modern (i.e., current day) Earth-like land–ocean distribution with orography and numerous initial atmospheric compositions, ranging from current day to preindustrialization, the latter of which we consider here. Horizontally, the simulation has a resolution of 1°875 by 2°5, which corresponds to 96 cells latitudinally (north–south) and 144 cells zonally (east–west). Vertically the simulation domain is split into 70 pressure levels distributed in $\log(P)$ space such that the number of pressure levels increases near the dynamically active surface. It has been modified by G. J. Cooke et al. (2023) to account for the effects of synchronous rotation (see that work for more details).

Coupling WACCM6/CESM2 with our cometary impact model also required that we add two new external forcing sources to the model: water and thermal energy. In both cases these external forcing terms take the form of a rate of material or thermal energy input as well as a time frame over which to apply this input. In the case of the water deposition we spread the material out both temporally, introducing the material over 10 Earth days, and spatially, spreading the material over nine columns centered on the substellar point. This "slow" and spread-out deposition is necessary in order to limit the water abundance gradient near the impact site. Higher abundance gradients induce numerical instabilities in the radiative transfer solver, leading to model termination.

The thermal energy deposition is a little more complicated to implement since CESM's physics solver does not accept a direct thermal power input. Instead the deposited thermal energy must be converted to a temperature tendency

$$\frac{dT}{dt} = \frac{dE}{dt} \cdot \frac{1}{\rho_a \mathcal{V} c_p}, \tag{7}$$

where $\mathcal{V}$ is the volume of the cell in which the thermal energy has been deposited and c_p is the specific heat capacity at constant pressure. To prevent the formation of large, numerically unstable temperature gradients near the impact site, we spread this thermal energy out in the same way as was done for the deposited water. The final temperature tendency

Table 2
Planetary Parameters of TRAPPIST-1e

Parameter	Value	Unit
Radius R	0.91	$R_\oplus$
Mass M	0.772	$M_\oplus$
Semimajor Axis a	0.0292	au
Orbital Period $P_{\rm orb}$	6.099	days
Obliquity ϵ	0	…
Eccentricity e	0	…
Peak Insolation I	900	W m^{-2}
Surface Gravity g	9.1454	m s^{-2}

Note. Taken from L. Delrez et al. (2018), S. L. Grimm et al. (2018), and E. Agol et al. (2021), with the mass and radius of the planet chosen to be consistent with those from the TRAPPIST-1 Habitable Atmosphere Intercomparison Program (T. J. Fauchez et al. 2022; T. J. Fauchez et al. 2021; D. E. Sergeev et al. 2022; M. Turbet et al. 2022).

profile that is used as our cometary heat deposition profile is shown in blue in Figure 1.

A more technical discussion of how water and thermal energy deposition is implemented in WACCM6/CESM2 can be found online.[6]

2.2.2. TRAPPIST-1e

Here, as our initial unperturbed reference state, we consider a TRAPPIST-1e-like planet with the substellar point fixed over the Pacific Ocean (see Figure 1 of F. Sainsbury-Martinez et al. 2024). Note that our model was evolved for over 300 yr before impact so as to ensure that any effects associated with the atmospheric dynamics settling into a tidally locked circulation regime have dissipated.

Briefly, TRAPPIST-1e is a terrestrial planet that remains a significant object of interest in the search for a habitable, Earth-like exoplanet. It is slightly smaller and less massive than the Earth, with a radius of 0.91 $R_\oplus$ and a mass of 0.772 $M_\oplus$, leading to a slightly weaker surface gravity of 9.1454 m s^{-2}. It also orbits significantly closer to its host star than the Earth does the Sun, with an orbital period of only ∼6.1 days. However, because TRAPPIST-1 is a cool M dwarf, the peak insolation that TRAPPIST-1e receives (900 W m^{-2}) is around 66% of that received by the Earth, placing it near the cooler edge of the habitable zone. To reproduce this insolation in our models we follow the work of G. J. Cooke et al. (2023) and rescale the TRAPPIST-1 spectrum of S. Peacock et al. (2019) such that the total integrated insolation matches that of TRAPPIST-1e. A summary of the planetary parameters of TRAPPIST-1e is given in Table 2.

3. Results

Our analysis of the isolated effects of cometary water and heat deposition (see the Appendix) suggested that, unlike in our previous hot-Jupiter studies (F. Sainsbury-Martinez & C. Walsh 2024), both components of the cometary material deposition can play a significant role in shaping the postimpact planetary atmosphere. As such, here we focus our discussion on a fiducial model that couples both components of the icy cometary impact with our tidally locked, terrestrial exoplanetary atmosphere.

3.1. Water Abundance and Mean Temperature

Figure 2 shows how the fractional water abundance (top row) and mean temperature (bottom) vary both shortly after impact (left column) and over the ∼20 yr required for the model atmosphere to reach a quasi–steady state (right column). Note that the increase in fractional water abundance between the postimpact and 1 month profiles in Figure 2 occurs because we are plotting monthly mean values, and the impact occurs part way through 1 month, leading to a reduced temporally averaged value.

Starting with the fractional water abundance, the top row of Figure 2 shows how even a single icy cometary impact can change the atmospheric water content, particularly at low pressures, and how these changes can persist for years postimpact. These profiles also reveal the role that vertical transport plays in the distribution of cometary material. As can be seen in Figure 2, most of the cometary water is delivered at pressures $>10^{-4}$ bar, yet after only 1 month of simulation time, we find a several order-of-magnitude increase in water abundance for all pressures $< 10^{-3}$ bar. Moreover, we know that this enhancement is associated with vertical transport as the initial thermally ablated water shows signs of rapid settling at low pressures before mixing from the mid-atmosphere replenishes this reservoir (see the top-left panel of Figure 2, which reveals a decrease in outer-atmosphere water abundance in the first few months postimpact).

On the other hand, the atmosphere near the surface exhibits almost zero mean response to the influx of water, despite the relatively weak drop-off in deposited mass between the breakup site and surface (Figure 1). This can be attributed to the density of the atmosphere, which increases rapidly as we approach the surface. As such, the same mass of water has a much smaller effect on the atmospheric composition near the surface compared to low pressures. However, the limited effect of cometary water deposition on the near-surface atmosphere does not mean that cometary impacts will not be observable as transmission spectra typically probe low-pressure regions, like the outer and midatmosphere where the effects of water deposition are largest (see Section 3.6).

The difference in response to the cometary water deposition of different layers of the atmosphere can also be seen in Figure 3. Here we plot the temporal evolution of the mean fractional water abundance and temperature in the outer atmosphere ($P < 10^{-5}$ bar—left), the midatmosphere ($10^{-5} < P < 10^{-2}$ bar—middle), and near the surface (referred to as the deep atmosphere, with $P > 10^{-2}$ bar—right). These pressure regions were chosen in order to emphasize the pressure dependence of the atmospheric response to a cometary impact. By comparing these profiles we can see how the largest "spike" in fractional water abundance can be found in the outer atmosphere; over 2 orders of magnitude 3 months postimpact, with significant enhancements persisting for at least 5 yr postimpact. On the other hand, the longest-lasting enhancement in atmospheric water can be found in the midatmosphere, with the fractional water abundance remaining significantly enhanced with respect to that found in our nonimpacted reference case for over 15 yr postimpact. Finally we also find a very slight enhancement in the near-surface water abundance shortly after the impact. Our analysis of the thermal energy deposition in isolation (Appendix A.2) suggests that the one driver of this deeper enhancement is an initial burst of cometary

---

[6] http://gitlab.com/leeds_work/cesm_comet/

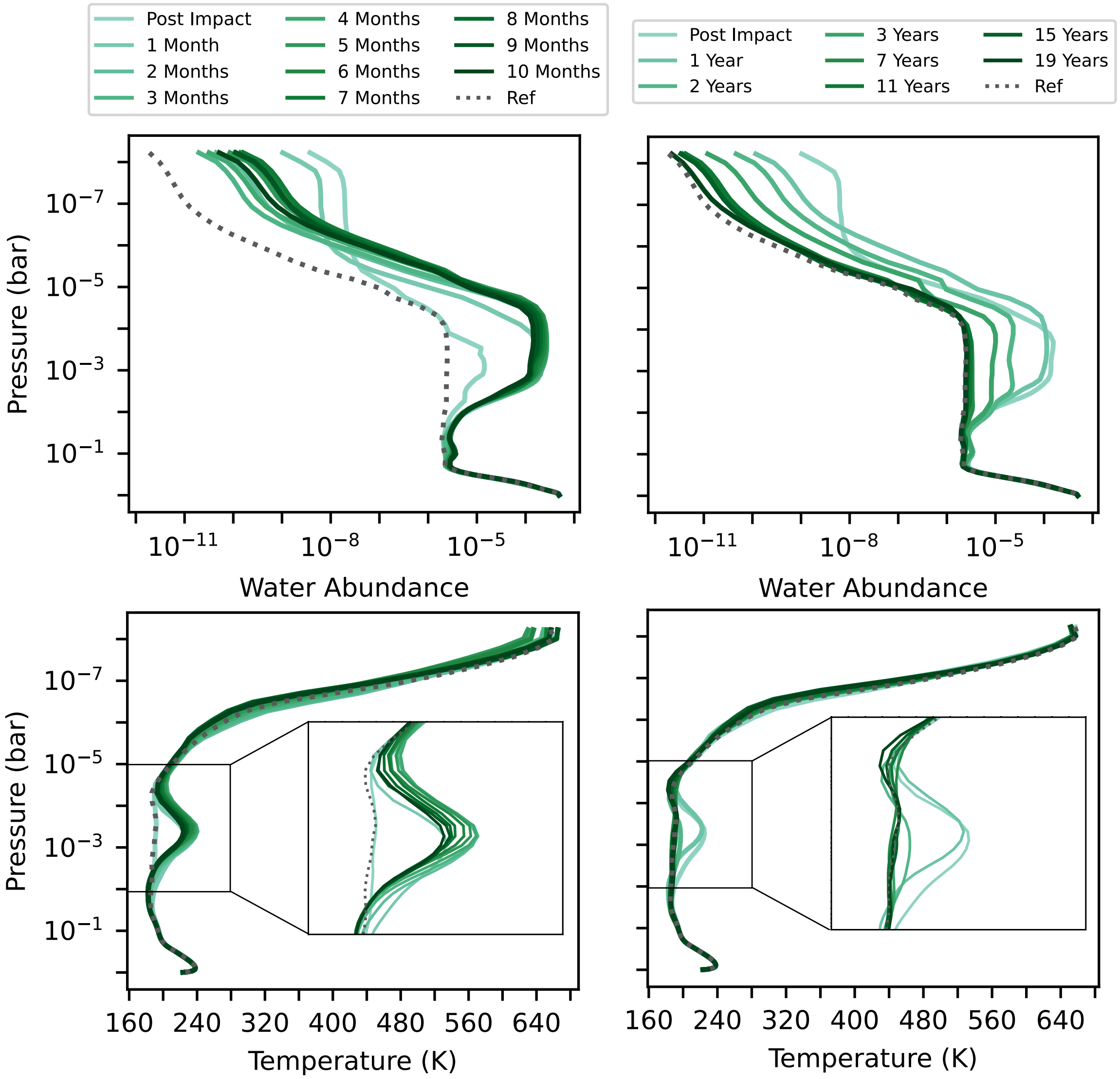

Figure 2. Fractional water abundance (top) and temperature (bottom) profiles showing the rapid atmospheric evolution within the first 10 months (left) of the impact of a pure water ice comet and the slower but steady settling of the atmosphere into a quasi–steady state (right) reminiscent of the nonimpacted reference state (gray dashed). Here each profile is calculated by averaging both horizontally over all latitudes and longitudes and temporally over 1 month of simulation time. To better demonstrate the change in temperature in the midatmosphere, we include an inset showing a zoomed-in view of the temperature profile between 10^{-2} and 10^{-5} bar.

heating–driven evaporation/sublimation of water droplets, ice, and snow, combined with the relatively weak water deposition.

The influx of a significant fraction of the cometary ice/water and thermal energy into the midatmosphere also has a significant effect on the local temperature. As shown on the bottom row of Figure 2, we find that a thermal inversion forms at $\sim 5 \times 10^{-4}$ bar (i.e., at the top of the stratosphere). At its peak in the resolved (i.e., nonaveraged) data, which is located at the substellar point, this temperature inversion is 35 K hotter than the same location in our nonimpacted reference case, and on average the midatmosphere is ∼15 K hotter (Figure 3). This heating occurs due to the opacity of the deposited water (S. Seager & D. D. Sasselov 2000; J. J. Fortney et al. 2008; A. Burrows et al. 2010; F. Sainsbury-Martinez & C. Walsh 2024), which causes an increased fraction of the incoming irradiation to be absorbed in the midatmosphere, driving localized heating.

This enhanced midatmosphere opacity, combined with albedo/scattering associated with clouds/ice (Section 3.3), also affects the near-surface temperature (Figure 3). We find that, despite the large amounts of thermal energy that the cometary breakup delivers (Figure 1/Section A.2), the reduction in flux reaching the (near)-surface drives a ∼1 K decrease in temperature. This cooling might have implications for planetary habitability in a theoretical scenario in which cometary impacts are sufficiently regular that the atmosphere remains optically thicker or has a higher albedo. As for how the thermal energy from the cometary impact has dissipated into the deep atmosphere, beyond a very short-lived temperature spike in the deep atmosphere (less than 1 month), most of it has contributed toward either balancing the aforementioned drop in insolation or driving (near)-surface water evaporation/sublimation. The latter effect can be seen when comparing the mean fractional water abundance in our fiducial model with its isolated deposition counterparts (see the Appendix).

Postimpact, we also find that the temperature of the outer atmosphere is slightly lower than our nonimpacted reference model. This effect can be linked with the slight shift in the

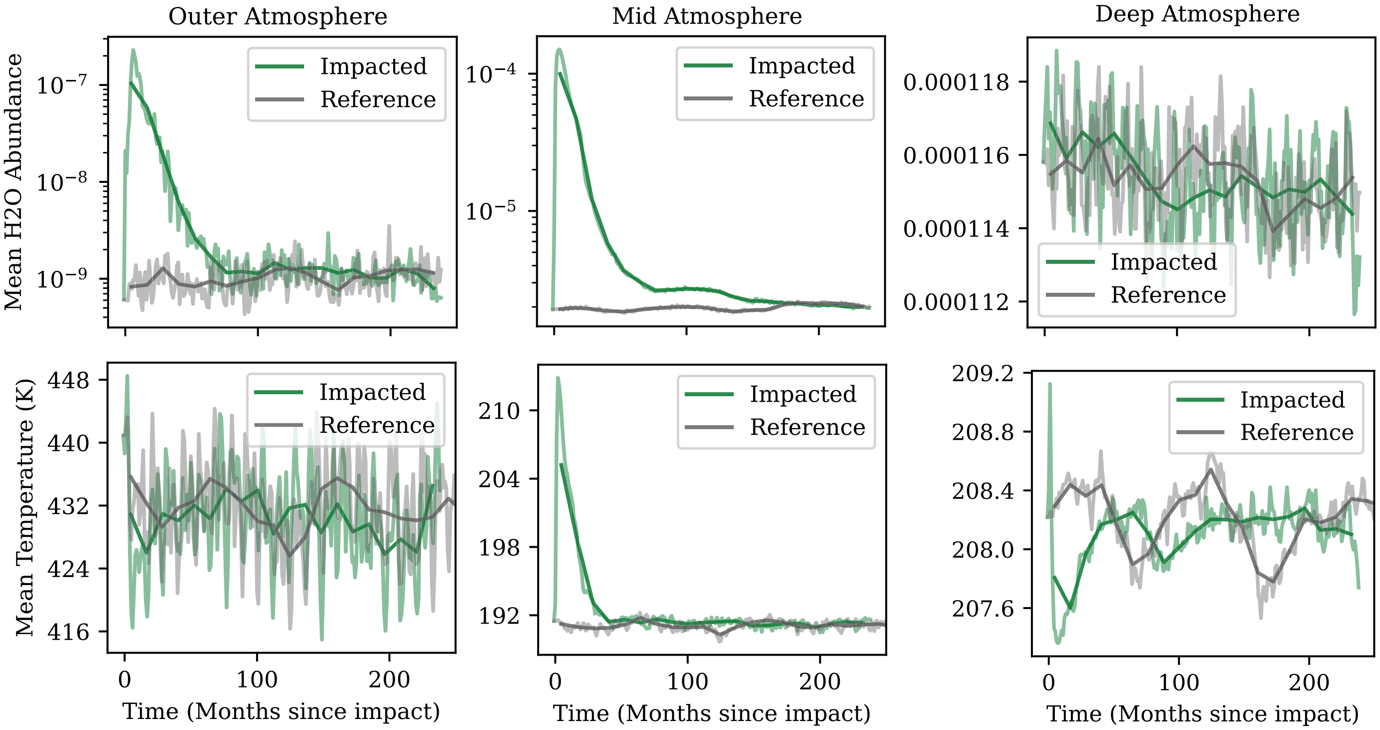

Figure 3. Time evolution of the annual mean (solid lines) and monthly mean (faint lines) fractional water abundance (top row) and temperature (bottom) in the outer atmosphere ($P < 10^{-5}$ bar—left), midatmosphere ($10^{-5} > P > 10^{-2}$ bar—middle), and near the surface ($P > 10^{-2}$ bar—right) of our fiducial coupled model (i.e., both water and thermal deposition—green) and our nonimpacted reference state (gray).

thermosphere to lower pressures/higher altitudes, an effect which itself is driven by the warming, and hence expansion, of the midatmosphere.

Finally, we note that the changes to the global mean temperature of the atmosphere are much shorter-lived than the changes to the fractional water abundance that drive them. This occurs due to a combination of the tidally locked nature of the illumination and the advection of water from the impact site (Section 3.2). The tidally locked illumination means that water-opacity effects are strongest on the dayside, particularly at the substellar point. Meanwhile, advective mixing of water vapor leads to the transport of deposited water from the insolated dayside to the dark nightside where it has only a very limited effect on the thermal properties of the atmosphere (acting as a greenhouse gas for outgoing irradiation). However, some long-lasting changes to the temperature structure of the atmosphere are present. For example, we find that the multiyear oscillations in atmospheric temperature (and water vapor content), which are associated with near-surface circulation cycles driven by the Earth-like orography and tidally locked insolation (similar cycles are found on the Earth; J. Lin & T. Qian 2022), have been shifted out of phase by the changes induced by our cometary impact. This suggests that even individual cometary impacts, particularly massive impacts, have the potential to drive long-lasting changes in the climate.

3.2. Advection of Water

The postimpact enhancement in fractional water abundance at low pressures suggests that transport plays a significant role in shaping how a cometary impact can affect atmospheric composition and chemistry. This conclusion is only reinforced by the strong global mean heating found in the midatmosphere, an effect that would not occur if the delivered water was confined to the impact site. As such, to better understand these effects, we next investigate the horizontal and vertical transport of water vapor.

We start by exploring the horizontal water vapor transport at a pressure of 2×10^{-2} bar. Note that we have chosen to focus our analysis on this pressure level due to the slower dynamical timescale of the deep atmosphere, which allows us to better explore each stage of the longitudinal and latitudinal transport of water vapor.

Figure 4 shows the fractional water abundance at nine different points in time, ranging from preimpact (top left), to near steady state 19 yr postimpact (bottom right). Initially water is deposited by the comet at and around the substellar point (top middle); however, almost immediately the strong zonal winds at this pressure level (see Figure 5) drive eastward advection. As such, a little over 2 months postimpact, we find that the impact-delivered water is almost completely longitudinally homogenized. This can be seen as a strong equatorial band of water vapor in the top-right panel of Figure 4. Note that this horizontal homogenization suggests that the results for cometary impacts at other equatorial longitudes should be similar to those found here, just slightly delayed (for example, the formation of the midatmosphere thermal inversion) to account for the advection of water from the impact site to the dayside. Due to the inherent differences in strength between longitudinal and latitudinal transport in tidally locked atmospheres, this equatorial water band persists for months postimpact. For example, the middle-left panel of Figure 4 reveals that, 6 months postimpact, latitudinal winds have only just started to break the longitudinal homogenization of the equatorial water band, with southward/northward advection slightly east/west of the substellar point, respectively. The

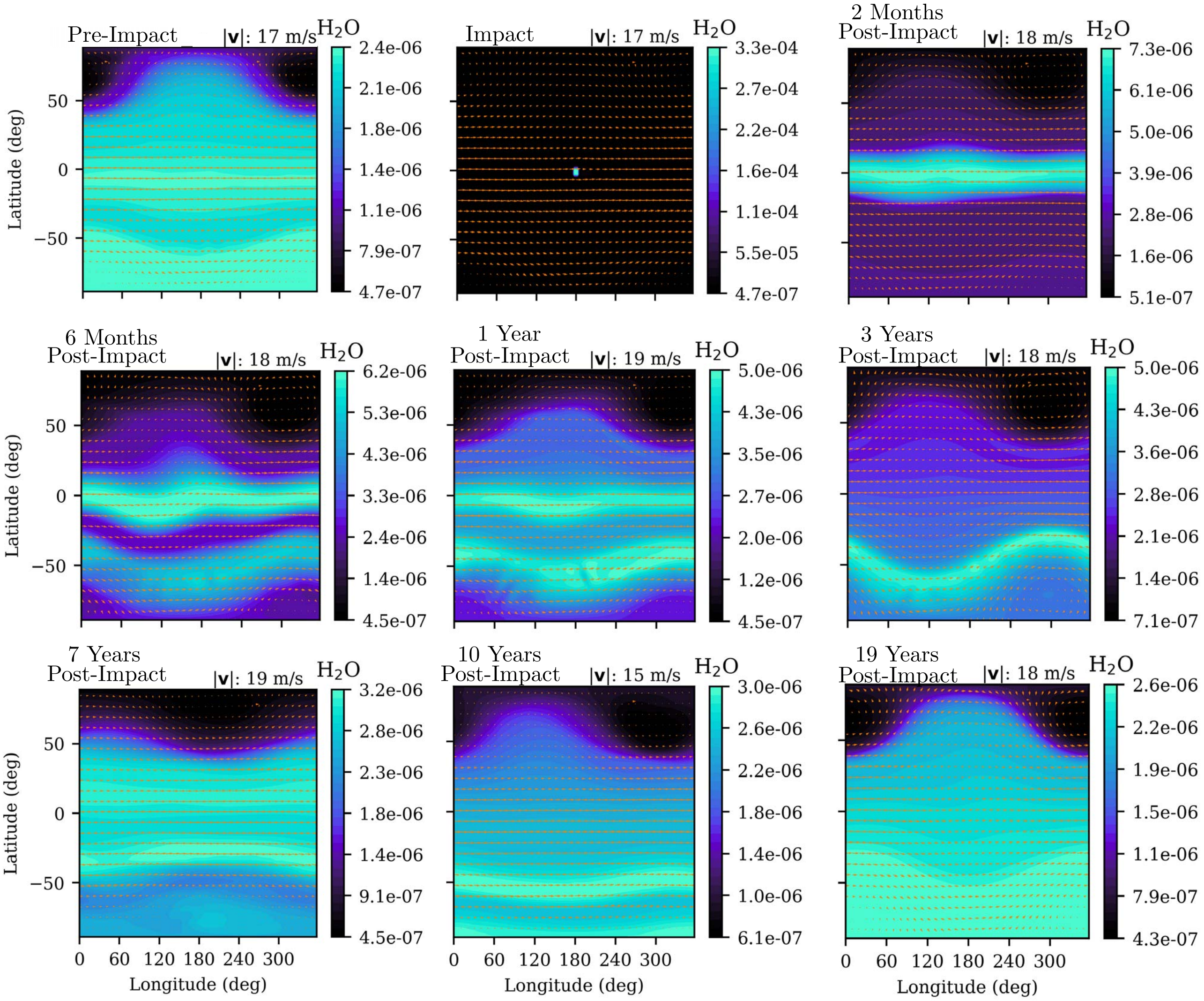

Figure 4. Horizontal slices of the fractional water abundance at a pressure of $P = 2 \times 10^{-2}$ bar (∼25 km above the surface), showing the transport of impact-delivered water from the substellar point both longitudinally (forming a equatorial band of water) and latitudinally (specifically toward the south pole) in our fiducial model. Note that this transport is closely associated with the horizontal wind, the mean ($|\boldsymbol{v}|$) of which is shown at the top right of each panel and that we plot using orange quivers. Moreover, note that the dynamic range of each color bar is different in order to highlight the change in water distribution with time.

difference in strength between longitudinal and latitudinal mixing remains apparent even as latitudinal winds advect the peak in the water abundance southward. For example, between 1 and 3 yr postimpact, shown on the center and middle-right panels of Figure 4, we find that a band of water vapor in the southern hemisphere with strong horizontal homogenization and that traces the shape of the off-equator winds, such as the nightside polar vortices. From here, latitudinal transport slowly breaks this southern water band up (bottom row of Figure 4), such that, 10–20 yr postimpact, we find an abundance profile which is similar, but not identical, to that found preimpact or in our nonimpacted reference case (top left). Note that the slight latitudinal shift in the abundance profile is likely linked to the delicate multiyear oscillations being out of phase with each other due to the disruptive effects of the cometary impact (Figure 3).

Note that the advection of the cometary impact–delivered water is similar to that found at 2×10^{-2} bar for most other pressure levels in our models. However, there are two exceptions. The first is that at very low pressures ($P < 2 \times 10^{-4}$ bar), the timescale of both longitudinal and latitudinal transport is short, and as such, water vapor is very rapidly mixed throughout the outer atmosphere. This has implications for observations since an increase in the opacity of these pressure levels can mask the rest of the atmosphere from spectroscopic transit observations (Section 3.6). On the other hand, as discussed in F. Sainsbury-Martinez et al. (2024), the presence of an Earth-like land mass distribution with its associated orography acts to drive the near-surface dynamics away from those associated with tidally locked insolation. At the same time, evaporation of the liquid ocean at the substellar point can also mask effects associated with a substellar cometary impact since the relative change in near-surface water abundance is small. Together these effects make an analysis of the near-surface water vapor particularly tricky, and since these pressure levels are unlikely to be probed via transit spectroscopy, we focus our efforts on lower pressure levels.

However the influence of orography on the atmospheric dynamics is still felt at lower pressures, albeit to a lesser extent than near the surface. As discussed in F. Sainsbury-Martinez et al. (2024), differences in the land mass distribution, as well as the orography of said land masses, between the northern and

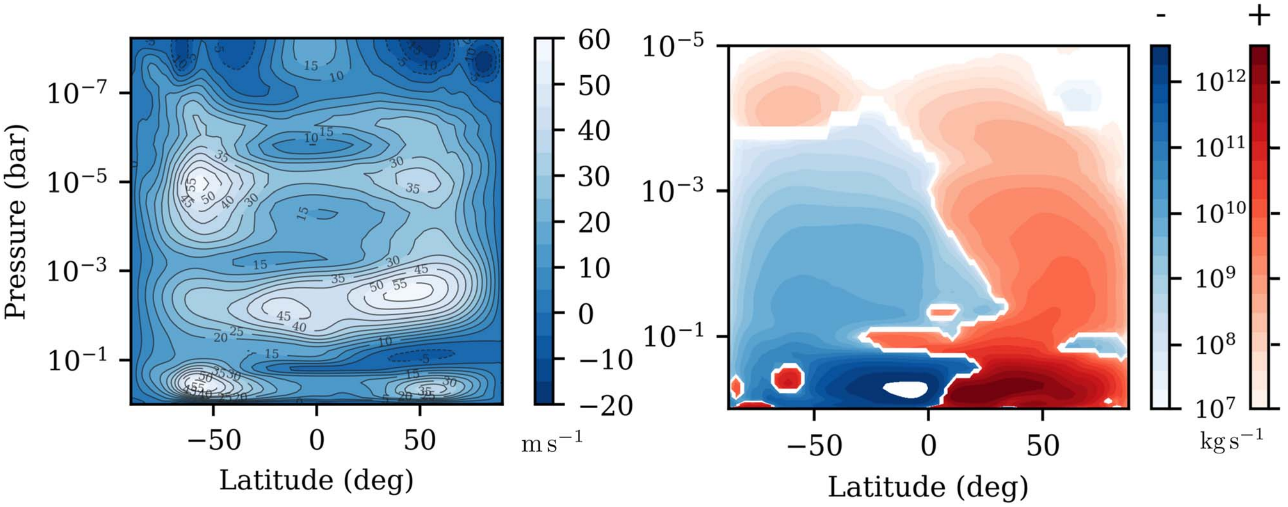

Figure 5. Zonally and temporally averaged zonal wind (left) and meridional circulation streamfunction (right) for our fiducial cometary impact model. Note that the meridional circulation profile is plotted on a log scale with clockwise circulations shown in red and anticlockwise circulations shown in blue. Thus, for example, we find that the clockwise cell in the northern hemisphere and the anticlockwise cell in the southern hemisphere combine to drive an upflow slightly north of the equator at all pressures greater than 10^{-5} bar. For $P < 10^{-5}$ bar, which we do not show due to the relative weakness of outer atmosphere circulations, we find a series of stacked circulation cells that alternate between clockwise and anticlockwise circulation with altitude.

southern hemispheres of the Earth and our Earth-like model can break the symmetry between northern and southern hemisphere winds and circulations. This can be seen in both the zonally averaged zonal wind and meridional circulation profiles, which we plot in Figure 5, and it can explain why our equatorial band of postimpact water is advected southward.

Starting with the zonally averaged zonal wind, differences in both the strength of the off-equator jets as well as their latitudinal location are apparent. For example, the jet in the southern hemisphere at 10^{-5} bar is not only ∼50% faster than its northern hemisphere counterpart but also a few degrees further from the equator. Moving deeper, to $\sim 5 \times 10^{-3}$ bar, we find that the situation is reversed. The jet in the northern hemisphere is now ∼10% faster than its southern counterpart, and the difference in latitudinal locations has grown. While the jet in the northern hemisphere is still centered around a latitude of 55°, the jet in the southern hemisphere is much closer to the equator (centered around −25°), so close that it extends across the equator and into low latitudes in the northern hemisphere. As such, any material deposited close to this pressure level, which includes a large fraction of the cometary water, will generally be associated with southern hemisphere dynamics. This can also be seen in the meridional circulation profile (see below). Finally, near the surface (∼0.5 bar), we find a pair of high-latitude jets with the jet in the southern hemisphere, which lies at a latitude which is broadly land mass free, being on average almost twice as fast as its northern counterpart.

The aforementioned preference for equatorial material to be associated with southern hemisphere dynamics is also reflected in the meridional mass streamfunction ψ, which takes the following form:

$$\psi = \frac{2\pi R_p}{g\cos\theta}\int_{P_{\rm top}}^{P_0} v\, dP, \tag{8}$$

where v is the latitudinal velocity, R_p is the radius of the planet, g is the surface gravity, θ is the latitude, and P_0 and $P_{\rm top}$ are the pressure at the surface and top of the atmosphere, respectively. The right-hand panel of Figure 5 shows the zonally averaged meridional circulation profile. Here clockwise circulations are shown in red and anticlockwise circulations are shown in blue. Where these circulations meet, net flows develop. For example, the clockwise circulation cell in the northern hemisphere and the anticlockwise circulation in the southern hemisphere combine to drive a net upflow slightly north of the equator for all $P > 5 \text{ x } 10^{-5}$ bar. As for the lower pressure regions of the atmosphere (not shown here due to the significantly weaker circulation strengths at low densities), we find stacked cells alternating between clockwise and anticlockwise circulation with altitude, hence explaining the efficient mixing of the outer atmosphere. The combination of this net upflow and efficient horizontal mixing in the outer atmosphere explains the rapid vertical mixing of deeply deposited material seen in Figure 2. The asymmetry between circulations in the northern and southern hemispheres explains the southward advection of equatorial water: at 10^{-2} bar an equatorial air parcels falls within the poleward (rising) region of the southern hemisphere's anticlockwise circulation cell; as such it is rapidly advected southward. In the same vein, material delivered by a cometary impact at slightly higher latitudes in the northern hemisphere might be expected to be advected northward.

3.3. *Effects of Water on the Broader Atmosphere*

Beyond acting as a source of heating in the midatmosphere, the water that an icy cometary impact delivers to the atmosphere also affects the atmospheric chemistry, composition, and climate. There are two main mechanisms by which this can occur: (i) the deposited water can, via photolysis, act as a source of atmospheric oxygen and hydrogen, tipping the balance in chemical reactions toward oxygen- and hydrogen-rich molecules; and (ii) the water can condense out of the atmosphere to form rain droplets, snow flakes, and ice crystals, all of which can contribute to both cloud formation and the scattering of incoming irradiation.

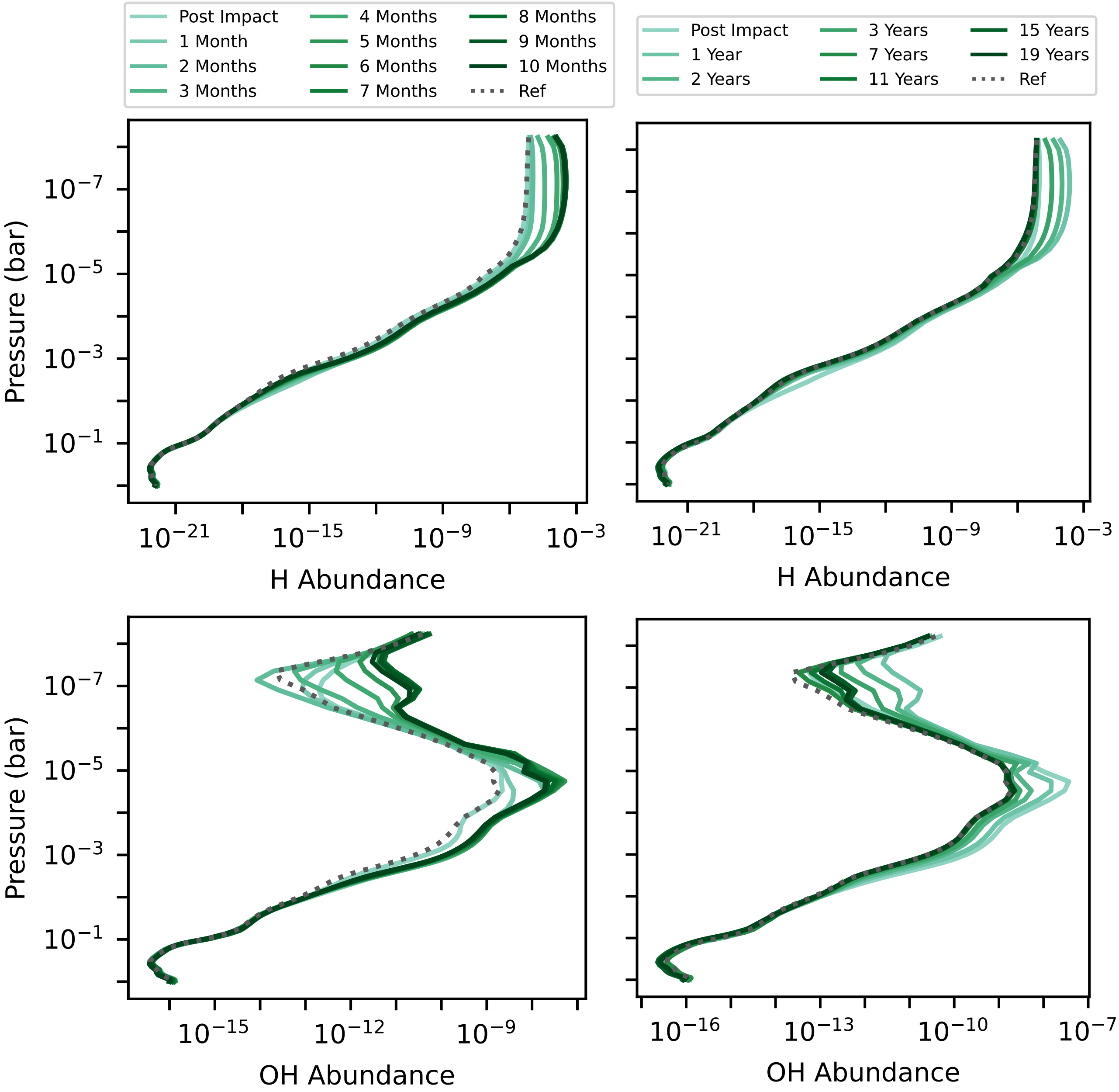

Figure 6. Fractional atomic hydrogen (H; top) and hydroxyl radical (OH; bottom) abundance profiles showing the products of the photolysis of the cometary-delivered water in our fiducial model. On the left we show the profiles within the first 10 months of impact, when the water content of the outer atmosphere is at its peak and hence photolysis is strongest, while on the right we show how, over 19 yr postimpact, the atmosphere settles toward a quasi–steady state close to our nonimpacted reference case (gray dashed).

3.4. Effects of Water on Composition

We start by exploring the effects of the deposited water on the atmospheric composition. Underlying these changes is the photodissociation of the deposited water vapor. We investigate the enrichment of the two products, which form due to one of the main UV photolysis reactions of water:

$$H_2O + h\nu \rightarrow H + OH, \tag{9}$$

where H is atomic and OH the hydroxyl radical. Figure 6 shows the change in fractional atomic hydrogen (top row) and hydroxyl radical (bottom) abundances both shortly after impact (left) and over the ∼20 yr required for the atmosphere to reach a quasi–steady state (right). Here we find that both molecules exhibit a slightly delayed enrichment, particularly the hydrogen abundance at low pressures. This delay occurs because the initial photolysis rate of the deposited water is slow and it takes time for the water to advect through the atmosphere: when the deposited water is confined to the impact site the rate of photolysis is low due to the low ratio of integrated UV flux to water vapor in such a confined region. However, as discussed in Section 3.2, the deposited water is rapidly mixed zonally and more weakly mixed latitudinally. This significantly increases the area in which UV irradiation can interact with cometary-delivered water, resulting in the 2 to 3 order of magnitude increase in peak atomic hydrogen and hydroxyl radical abundance seen in Figure 6. The abundance of both molecules then drops due to a combination of further chemical reactions, such as the formation of molecular hydrogen (H_2; Figure 7) or

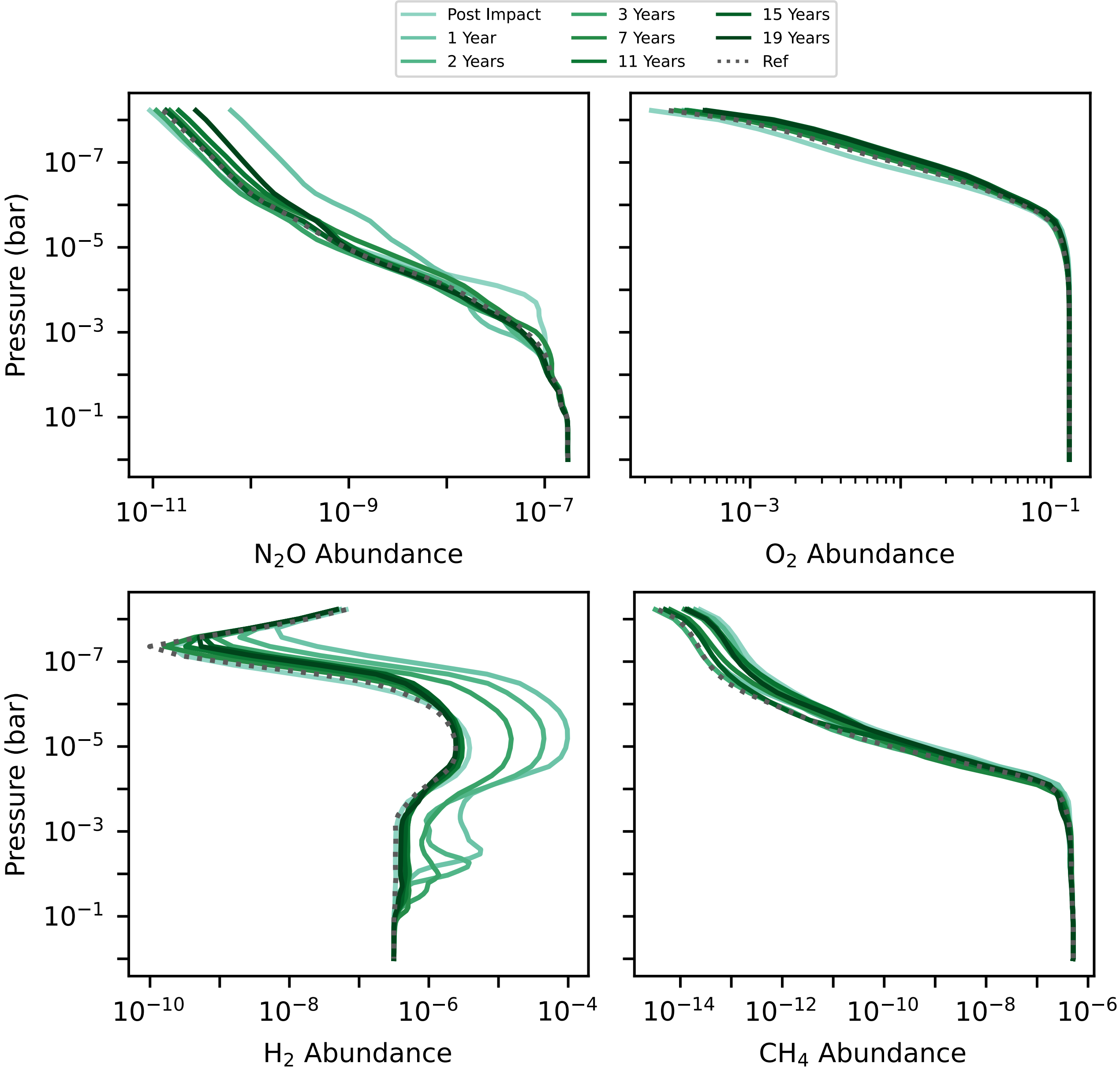

Figure 7. Fractional nitrous oxide (N_2O; top left), molecular oxygen (O_2; top right), molecular hydrogen (H_2; bottom left), and methane (CH_4; bottom right) abundance profiles for a selection of molecules whose abundance is enhanced due to the impact-driven enrichment of atmospheric oxygen (top) or hydrogen (bottom). Here each profile is calculated by averaging both horizontally over all latitudes and longitudes and temporally over 1 month of simulation time, and we compare each profile with that found in our nonimpacted reference state (gray dashed).

hydroperoxyl radicals (HO_2; Figure 8), and a slowing of the water photolysis rate as water vapor is advected toward to the dark nightside and poles, as well as raining/snowing/freezing out of the atmosphere. This drop is more rapid than the decrease in water abundance in the outer and midatmosphere (Section 3), suggesting that there is a nonlinear relationship between water abundance and the rate of water photodissociation. This can be linked back to the opacity of water: when the fractional water abundance is very high ($\gtrsim 10^{-5}$), the midatmosphere becomes optically thick, and hence most of the incoming UV irradiation is absorbed by water, leading to strong photodissociation. However, as the water abundance drops, so too does the associated opacity, and hence some of the incoming UV irradiation can be absorbed by other photosensitive molecules, such as ozone (O_3) or the hydroxyl radical (OH).

Note that WACCM6/CESM2 includes both a wide range of photodissociation pathways and a number of reaction pathways via which oxygen can be freed from hydroxyl radicals, such as the formation of hydroperoxyl radicals via the destruction of ozone—$OH + O_3 \rightarrow HO_2 + O_2$. For more details, see Table S2 of L. K. Emmons et al. (2020), which lists every (photo) chemical reaction included in our model.

As discussed above, the photodissociation of cometary impact–delivered water and the resulting products changes the overall composition of the atmosphere, enhancing the fractional abundance of oxygen-rich and hydrogen-rich molecules. Four examples of molecules that increase in abundance due to this enhancement are shown in Figure 7; nitrous oxide (N_2O; top left), molecular oxygen (O_2; top right), molecular hydrogen (H_2; bottom left), and methane (CH_4; bottom right).

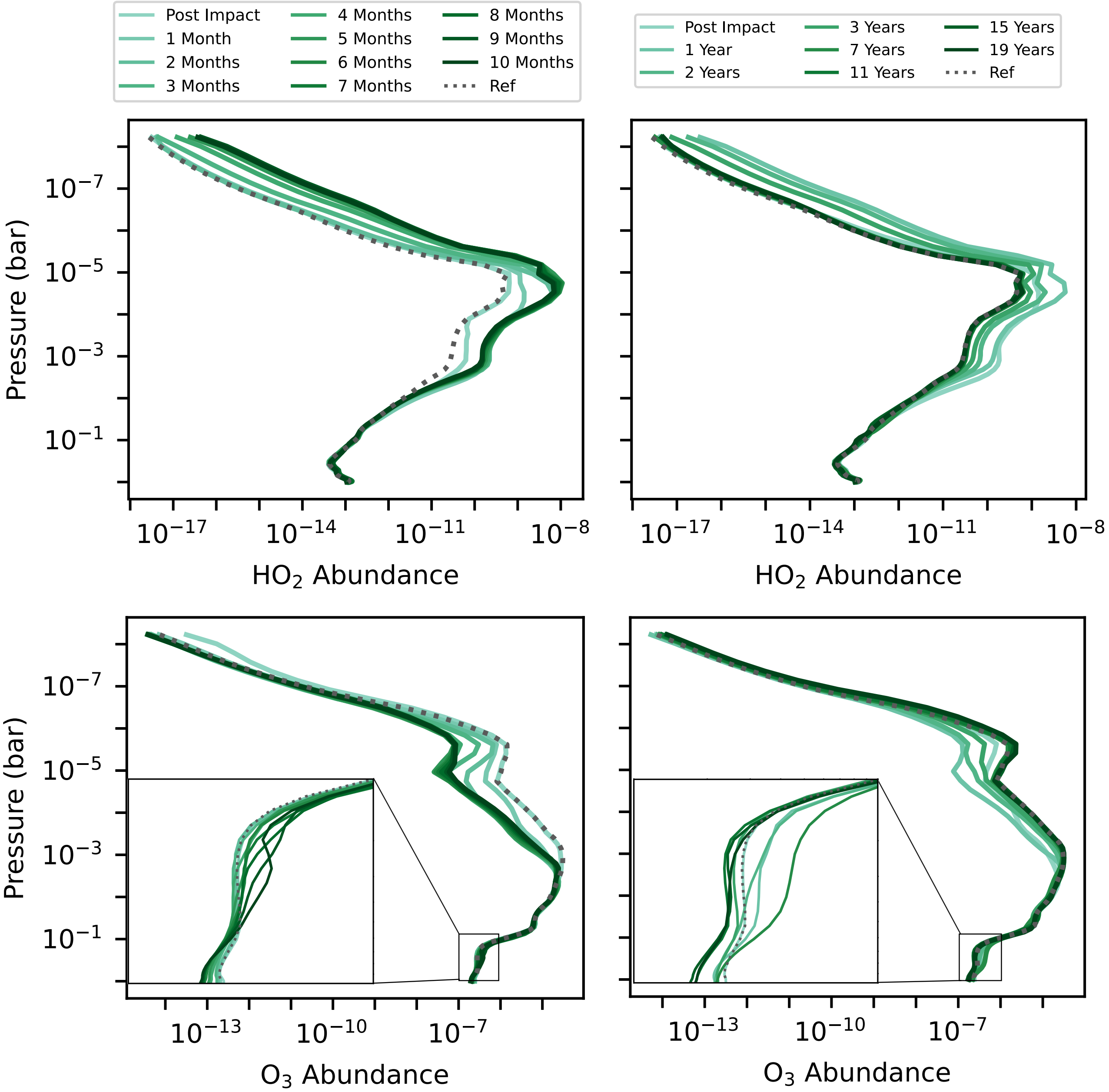

Figure 8. Fractional hydroperoxyl radical (HO_2; top) and ozone (O_3; bottom) abundance profiles showing how the increase in atmospheric oxygen abundance associated with the cometary impact does not necessarily lead to the formation of ozone. Instead we find that it actually results in a decrease in ozone abundance due to the formation of molecules associated with catalytic ozone destruction. Here we show how these molecules evolve over the first 10 months postimpact (left), when water photolysis is strongest, and over 19 yr postimpact as the atmosphere settles toward a quasi–steady state close to that found in our nonimpacted reference state (gray dashed). To better demonstrate the change in ozone abundance near the surface, we include an inset showing a zoomed-in view of the fractional ozone abundance profile between 1 and 0.1 bar.

We start with nitrous oxide (top left), which shows a strong enhancement for $P \lesssim 5 \text{ x } 10^{-4}$ bar 1 month postimpact, when the photochemically driven oxygen enhancement is at its peak. However, except at the very lowest pressures where the total number of molecules is low, we find that this enhancement does not persist. This is again due to photochemistry: throughout the dayside, except near the surface, which is mostly shielded, we find that the incoming UV irradiation drives photodissociation of nitrous oxide, leading to the formation of molecular nitrogen (N_2), molecular oxygen (O_2), and nitrogen monoxide (NO). A similar result, vis-à-vis an initial peak in abundance followed by photochemical destruction, is also found, for example, for nitrogen dioxide (NO_2), nitrate (NO_3), and to a lesser extent hydroperoxyl radicals (HO_2; see Figure 8). As we discuss below, there is another mechanism by which these molecules can be destroyed: reacting with and destroying ozone. Together, these mechanisms can drive nonlinear changes in fractional abundance, particularly when abundances, or the local atmospheric density, are low.

We also find that the fractional abundance of molecular oxygen (O_2; top right) also increases due to the oxygenation of the atmosphere. However, due to the high abundance of O_2 (it is the second most abundant molecule in an Earth-like /exo-Earth atmosphere), the observed changes in abundance are both relatively small and confined to lower pressure regions where O_2 molecules have a lower density. As such, it is unlikely that the change in O_2 abundance due to an individual cometary impact would be observable, even discounting the effects that a massive increase in water vapor has on the atmospheric opacity (see Section 3.6). Note however that the fact that the O_2 abundance of the atmosphere is enhanced at all suggests that cometary impacts may be an important means of delivering oxygen to young planets that start life in an oxygen-poor state (i.e., with a reducing atmosphere).

We finish with two molecules that experience an enhancement due to the impact-driven enrichment of atmospheric hydrogen: molecular hydrogen (H_2), which we plot on the bottom left of Figure 7, and methane (CH_4), which we plot on the bottom right. The postimpact enhancement of H_2 is relatively simple to understand: not only does one of the photodissociation pathways of water directly lead to the formation of H_2, but other photolysis products (H/OH) also undergo reactions that lead to the formation of H_2. As as result we find a strong enhancement in H_2 that persists for up to 10 yr postimpact.

The enrichment in atomic hydrogen and hydroxyl radical abundance due to the cometary impact can also lead to the formation of methane via the destruction of, for example, formaldehyde (CH_2O). This process is reinforced by the opacity of water, reducing the UV-driven photodissociation of methane. However, the limited number of reaction pathways that lead to the formation of methane, as well as the low density of the molecules involved, means that the enhancement is generally limited and delayed with respect to the impact.

There is one major exception to the impact-driven enhancement in the abundances of oxygen-bearing molecules: ozone (O_3). Rather than being enhanced, we instead find significant ozone depletion in the midatmosphere, especially around 10^{-5} bar. This can be seen in Figure 8, which shows the change in the fractional abundance of ozone (bottom row) and hydroperoxyl radical (top row) both shortly after impact (left) and over the ∼20 yr required for the atmosphere to reach a quasi–steady state (right).

Here, as shown on the bottom row of Figure 8, we find a 2 order of magnitude depletion in ozone abundance between 3 to 4 months postimpact. Furthermore, even though this depletion is primarily in the midatmosphere and our models reveal an initial, weak, enhancement in the near-surface ($P > 10^{-1}$ bar) ozone postimpact, we find that, for the first 5 yr postimpact, the average ozone column density has dropped by ∼7.5% from $\sim 7.7 \times 10^{23}$ to $\sim 7.1 \times 10^{23}$ molecules m^{-2}. This destruction, as well as the slight postimpact deep enhancement, can be linked to the cometary delivery of water.

As discussed above, the oxygenation of the atmosphere by cometary material leads to the formation of NO_x and HO_x, families of molecules, which play a key role in the destruction of ozone on the Earth. For example, hydroperoxyl radicals (HO_2), which are thought to be responsible for around half of ozone destruction in the Earth's atmosphere (P. O. Wennberg et al. 1994), exhibit a significant increase in abundance, over 1 order of magnitude, throughout the outer and midatmosphere ($P < 10^{-3}$ bar). This enrichment occurs because there are numerous reaction routes via which these molecules can form, including pathways that result in the destruction of ozone, such as

$$O_3 + OH \rightarrow HO_2 + O_2. \tag{10}$$

The hydroperoxyl radicals that form from this pathway can also destroy ozone,

$$O_3 + HO_2 \rightarrow OH + 2O_2, \tag{11}$$

leading to a chain reaction, including a catalytic hydroxyl radical–driven ozone destruction cycle and the strong correlation between the hydroperoxyl radical enhancement and ozone depletion shown in Figure 8. This cycle of NO_x/HO_x formation and ozone depletion weakens as the water photolysis rate drops (Figure 6) until approximately 7 yr postimpact, where we find a fractional ozone abundance that is similar to our nonimpacted reference state. Note, however, that there is an exception to this at very low pressures, where we instead find a weak but persistent enhancement. This enhancement is likely associated with the slight increase in the overall oxygen content of the atmosphere adjusting the balance between ozone destruction and formation.

Similarly, midatmosphere water photolysis is also responsible for the slight enhancement in near-surface ozone between 6 months and 3 yr postimpact. This is because the deposited water acts as both a strong source of opacity, shielding lower altitudes from the incoming (UV) radiation, thus shielding deep ozone from photodissociation, and a source of free O, which can react with O_2 to form ozone. However, as the water content of the midatmosphere drops, so too does its opacity, leading to the UV irradiation once again penetrating into the deep atmosphere and a steady drop in the near-surface ozone abundance.

3.5. Effects of Water on Climate

As an Earth system model, WACCM6/CESM2 includes a robust treatment of not only atmospheric chemistry and dynamics but also the climate, including cloud formation and precipitation, i.e., rain and snow. Since, for an Earth-like atmospheric composition, the primary constituent of both is water, it can be inferred that they will be significantly affected by an icy cometary impact.

In Figures 9 and 10 we plot the zonally and temporally averaged snow fraction, which represents the fraction of each cell's mass that is made up of snow, and cloud fraction, which represents the fraction of each cell that is covered by clouds at three different points in time postimpact, comparing our profiles with our nonimpacted reference state. In both cases we find significant changes associated with the cometary impact–delivered water. These changes are most visually apparent in the snow fraction profile, where we find a massive increase, greater than 10 orders of magnitude, in snow fraction at almost all pressure levels <0.1 bar. This is significant enough that low-pressure snow (and ice) now makes up a measurable fraction of the outer and midatmosphere, unlike the reference case where the presence of similar snow fractions is limited to near-surface regions. As we discuss in Section 3.6, this enhancement in low-pressure snow and cloud ice particles can have significant implications for the observed transmission spectra.

The only exception to the above increase in snow fraction is found for pressures slightly greater than 10^{-3} bar, where we instead find a strong dip associated with cloud formation and the shift of atmospheric water from snow/ice to clouds. Note, however, that the dip that occurs here is somewhat artificial: in its current form, WACCM6/CESM2 only models clouds for

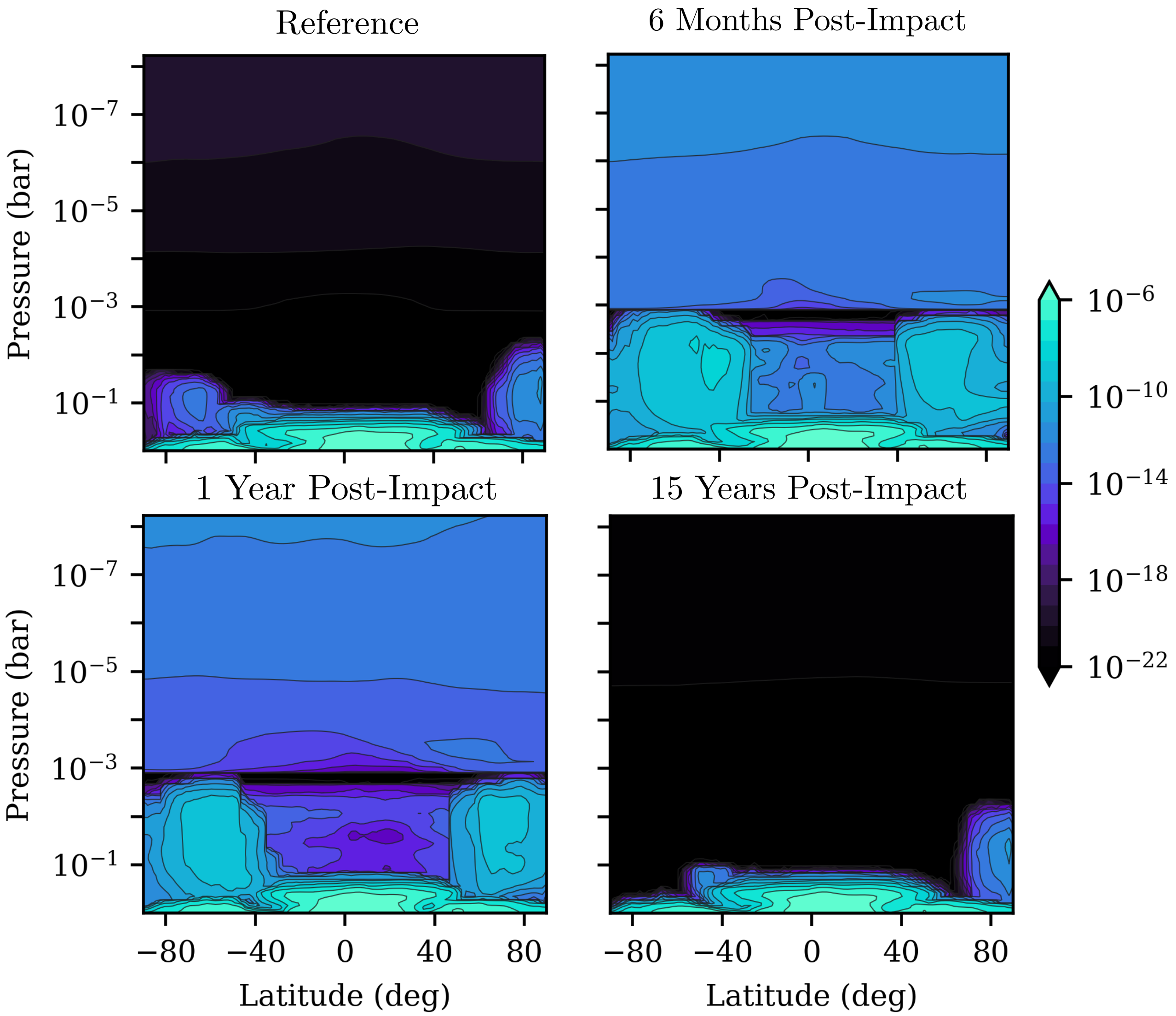

Figure 9. Zonally and temporally averaged snow fraction for our nonimpacted reference model (top left) and at three points in time postimpact for our fiducial model: 6 months (top right), 1 yr (bottom left), and 15 yr (bottom right) postimpact, by which time the impacted models' snow fraction has returned to a state close to that found in our reference state.

pressures $>10^{-3}$ bar. Cloud formation also explains the differences in the time evolution of the snow fraction above and below this level, with the atmosphere returning toward the nonimpacted reference state faster for pressures $>10^{-3}$ bar.

Evidence for cloud formation between 10^{-1} and 10^{-3} bar can be seen in the cloud fraction profile (Figure 10). Here we find significant cloud formation near the poles, with the cloud fraction reaching one between 10^{-1} and 10^{-3} bar at the north pole. These high-altitude off-equator/polar clouds form due to the condensation of impact-delivered water vapor in polar vortices and cold nightside Rossby gyres, the latter of which are similar to those found by M. Braam et al. (2023). However, nearer the surface, $P > 10^{-1}$ bar, we find that orography breaks up these water vapor–confining circulations (F. Sainsbury-Martinez et al. 2024), and instead the main driver of cloud formation is ocean evaporation at the substellar point—hence the equatorial cloud patch found at ∼0.5 bar.

Since the formation of high-altitude clouds is so closely tied to the water vapor enrichment of the midatmosphere, we find that, as this enhancement drops, so too does the high-latitude cloud fraction. While the drop seen in the first year postimpact is fairly rapid, it takes approximately 15 yr for the cloud fraction profile in our fiducial model to return to a state reminiscent of our nonimpacted reference state (bottom right).

It is important to note that, while cloud formation might be expected to have an effect on the planetary albedo by increasing the fraction of the incoming irradiation that is reflected, the high-latitude and/or nightside formation location of these impact-induced clouds means that any effect will be limited. In fact, one might expect that the clouds would instead cause the surface to warm due to their greenhouse effect, and indeed an analysis of the long-wave cloud forcing, which measures the greenhouse effect of clouds due to absorption and reemission of outgoing radiation, suggests that this is the case. For example, in the first 6 months postimpact, we find a ∼10% increase in the long-wave cloud forcing. However the observed cooling of the deep atmosphere postimpact suggests that the drop in near-surface heating due to high-altitude water vapor absorbing incoming irradiation on the dayside counters this warming greenhouse effect.

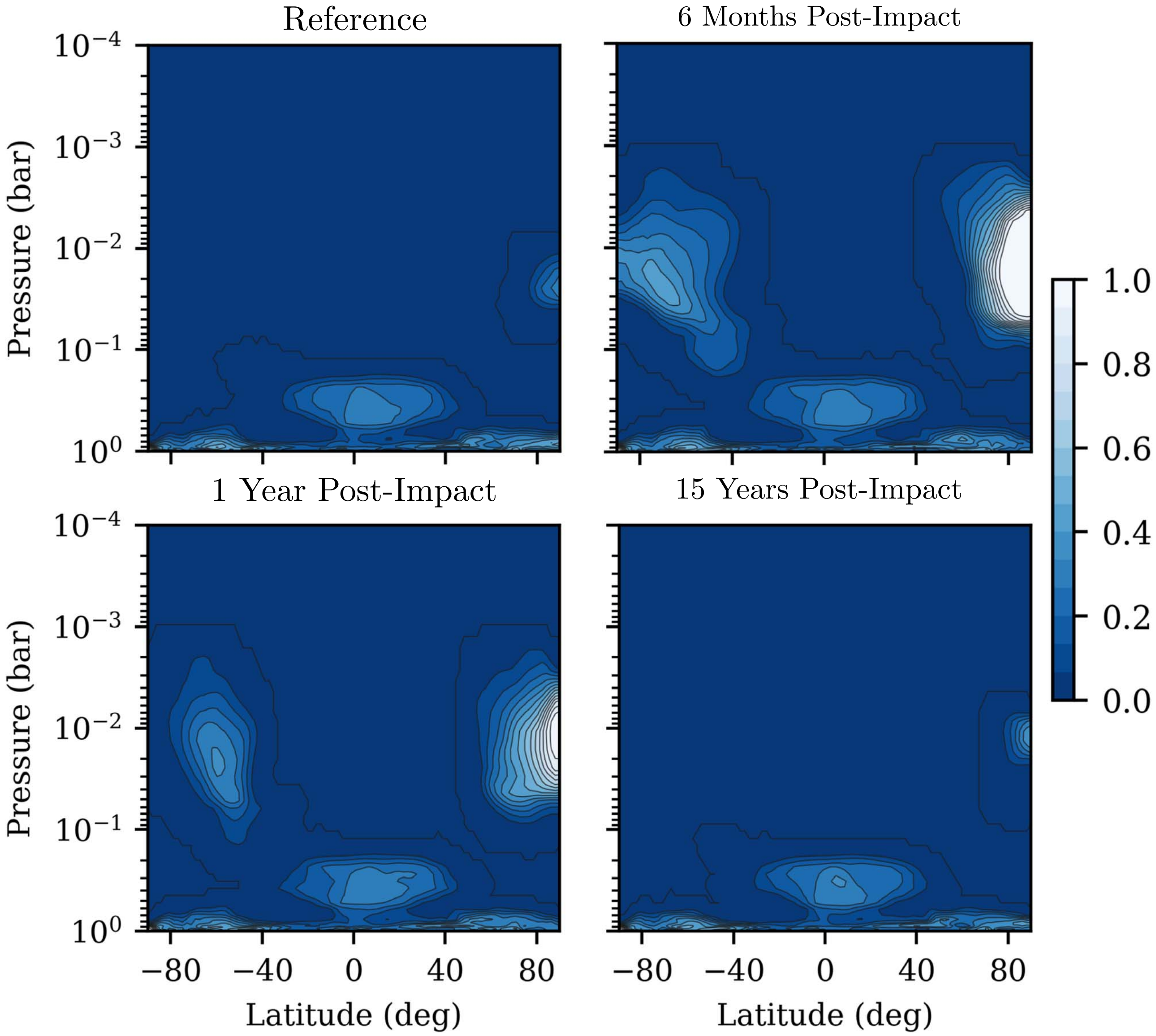

Figure 10. Zonally and temporally averaged cloud fraction for both our nonimpacted reference state (top left) and at three points in time postimpact for our fiducial model: 6 months (top right), 1 yr (bottom left), and 15 yr (bottom right) postimpact, by which time the impacted models cloud fraction has returned to that found in our nonimpacted reference state. Here we limit our plots to pressures $>10^{-4}$ bar due to the limited pressure range ($P > 10^{-3}$ bar) that the CESM cloud model operates over.

3.6. Observational Implications

We finish by investigating if the changes in atmospheric chemistry, composition, and climate that result from the impact of a single pure water ice comet (with $R = 2.5$ km and $\rho = 1$ g cm^{-3}) with a tidally locked Earth-like exoplanet might be observable. To do this we use the Planetary Spectrum Generator (PSG; G. L. Villanueva et al. 2018) to calculate idealized transmission and thermal emission spectra at four points in time postimpact, comparing these spectra with a corresponding spectra calculated using our nonimpacted reference state. We use the GlobES 3D mapping tool to compute transmission and thermal emission spectra between 0.2 and 20 μm using 3D data from a 5 day temporal-average snapshot. These spectra are binned both spectrally, such that spectral resolution is $R = 250$, and spatially. This is necessary to both reduce the file size given to PSG as well as the computational resources required to calculate a transmission or emission spectrum from 3D data. We regrid the data used to calculate the spectra to a 10° resolution longitudinally while leaving the latitudinal resolution unchanged (as this has the largest effect on transmission spectra). Note that we do not plot the emission spectrum between 0.2 and 4 μm due to a lack of any significant emission in this region. The thermal emission for TRAPPIST-1e only becomes significant for wavelengths >8 μm (J. Staguhn et al. 2019) due to the planet's low equilibrium temperature ($\sim$240 K).

The resulting transmission and thermal emission spectra are shown in Figure 11. Here we plot spectra at four points in time postimpact (green), comparing them with a corresponding spectra calculated from our nonimpacted reference case (gray). To aid in our analysis, we also include labels indicating a number of spectroscopic features of interest such as those associated with water (H_2O), carbon dioxide (CO_2), methane (CH_4), nitrous oxide (N_2O), oxygen (O_2), and ozone (O_3).

We start with the transmission spectra calculated 2 months postimpact, after the deposited water has started to mix

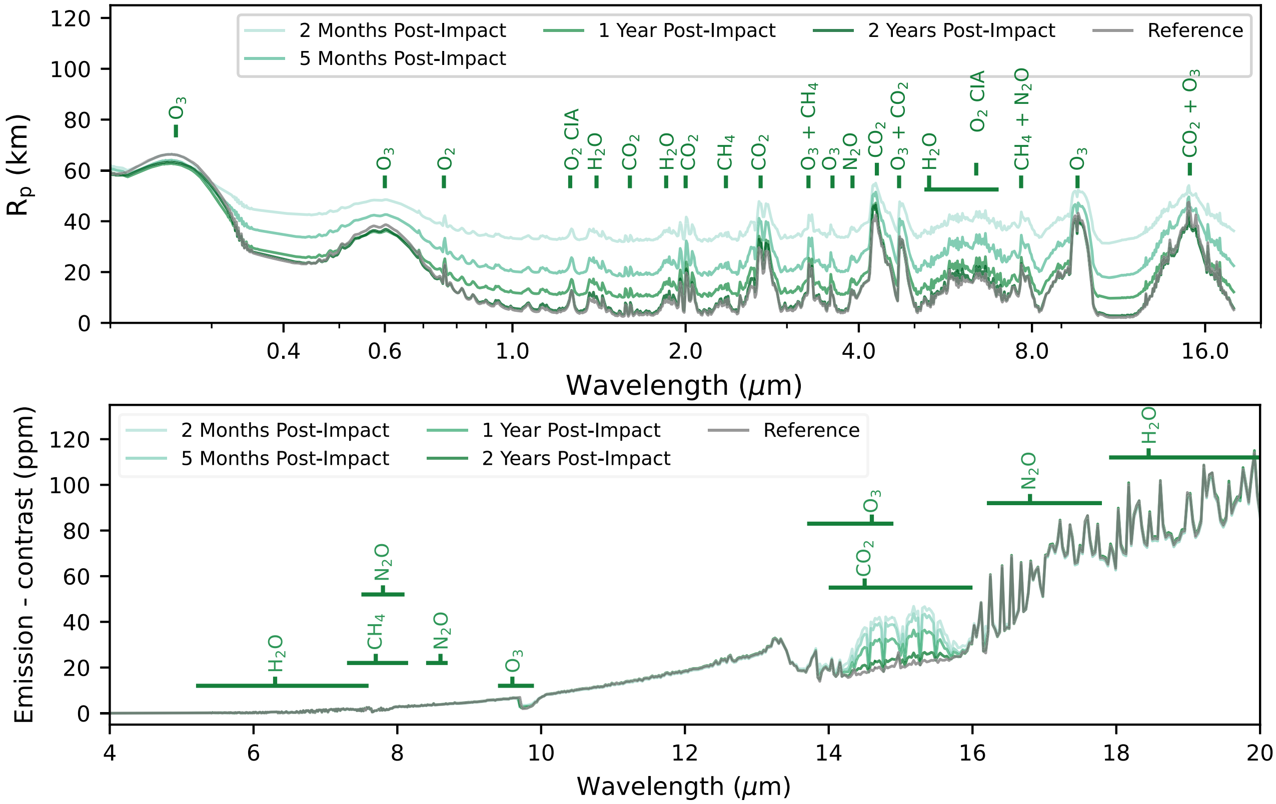

Figure 11. Example transmission spectra (top), in units of transit atmospheric thickness (R_p), and emission spectra, in units of contrast (radiance ratio with respect to the host star in parts per million), calculated with PSG using 3D data from the fiducial cometary impact model at four different points in time postimpact: 2 months, 5 months, 1 yr, and 2 yr. We also include a reference spectra, in gray, calculated using PSG using data from our nonimpacted reference state. To aid in interpretation, we have labeled a number of spectroscopic features of interest, including lines associated with H_2O, CO_2, CH_4, N_2O, O_2, and O_3. The emission spectra are calculated at a phase of 90°, i.e., midway between primary and secondary eclipse, which was chosen to be representative of the "average" case/emission. Note that we do not include any spectra calculated at earlier times in our impacted models due to instabilities in PSG caused by scattering associated with the high water content of the very outer atmosphere.

throughout the outer atmosphere. Here we find a near-uniform (for wavelengths > 0.8 μm) increase in the apparent thickness of the atmosphere (~38 km) when compared to our nonimpacted reference state (~14 km). This suggests that our transmission spectra is probing the lowest pressure regions of our atmosphere, a conclusion that is reinforced by the suppression of almost all spectral features, a suppression that occurs because the densities of many absorbers in the probed region are low. But why are our transmission spectra probing such a low-density region postimpact? The answer lies in the formation of snow (Figure 9) and cloud ice. The latter is shown in Figure 12, where we plot the zonally averaged cloud ice mixing ratio at three different points in time postimpact, comparing these profiles with our nonimpacted reference case. Here we find that the water delivery associated with an icy cometary impact drives the formation of significant quantities of cloud ice at pressures $<10^{-3}$ bar. Specifically, we find that the fraction of the atmosphere that is made up of cloud ice has gone from being insignificant to a few tenths of a percent. While this still represents a small fraction of the atmosphere, it is enough to scatter a significant fraction of the incoming radiation from the host star, leading to the observed increase in "continuum" level and hence apparent atmospheric thickness, in our transit spectra. Note that the scattering-driven increase in the apparent radius of a planet post a recent impact should be identifiable from a single transit observation when comparing the apparent radius with preimpact or follow-up observations.

With time, this cloud ice slowly settles, evaporates, and/or rains and snows out, decreasing the strength of this scattering effect and allowing us to probe lower-altitude, denser regions of the atmosphere. For example, 5 months postimpact, we find that between 1 and 18 μm our transmission spectrum now probes an average altitude of ~28 km above the surface, and spectral features associated with all of the aforementioned species are stronger, albeit still somewhat suppressed, relative to our reference state due to the relatively low densities probed.

At 1 yr postimpact, between 1 and 18 μm, we find that the transmission spectrum now probes an average altitude of ~ 19 km, which is only slightly higher than our nonimpacted reference state (~ 14 km), allowing for compositionally driven differences in spectroscopic features to become more apparent. For example, we tend to find that the strengths of water features, such as those found at 1.4, 1.9, or between 5.2 and 7 μm, are similar between our 1 yr (and 5 month) postimpact and reference models. This suggests that, in our impacted model, the enhancement in fractional water abundance balances the drop in probed atmospheric density. On the other hand, the strengths of ozone (O_3) features, such as those at 0.6 or 9.6 μm, are clearly reduced, with the former actually being weaker than our reference case and the latter only resulting in slightly higher apparent radii than the nonimpacted reference state despite the still-significant differences in continuum level. A similar story, of a slight suppression of feature strength, holds true for other absorbers, likely due to the slightly lower densities probed,

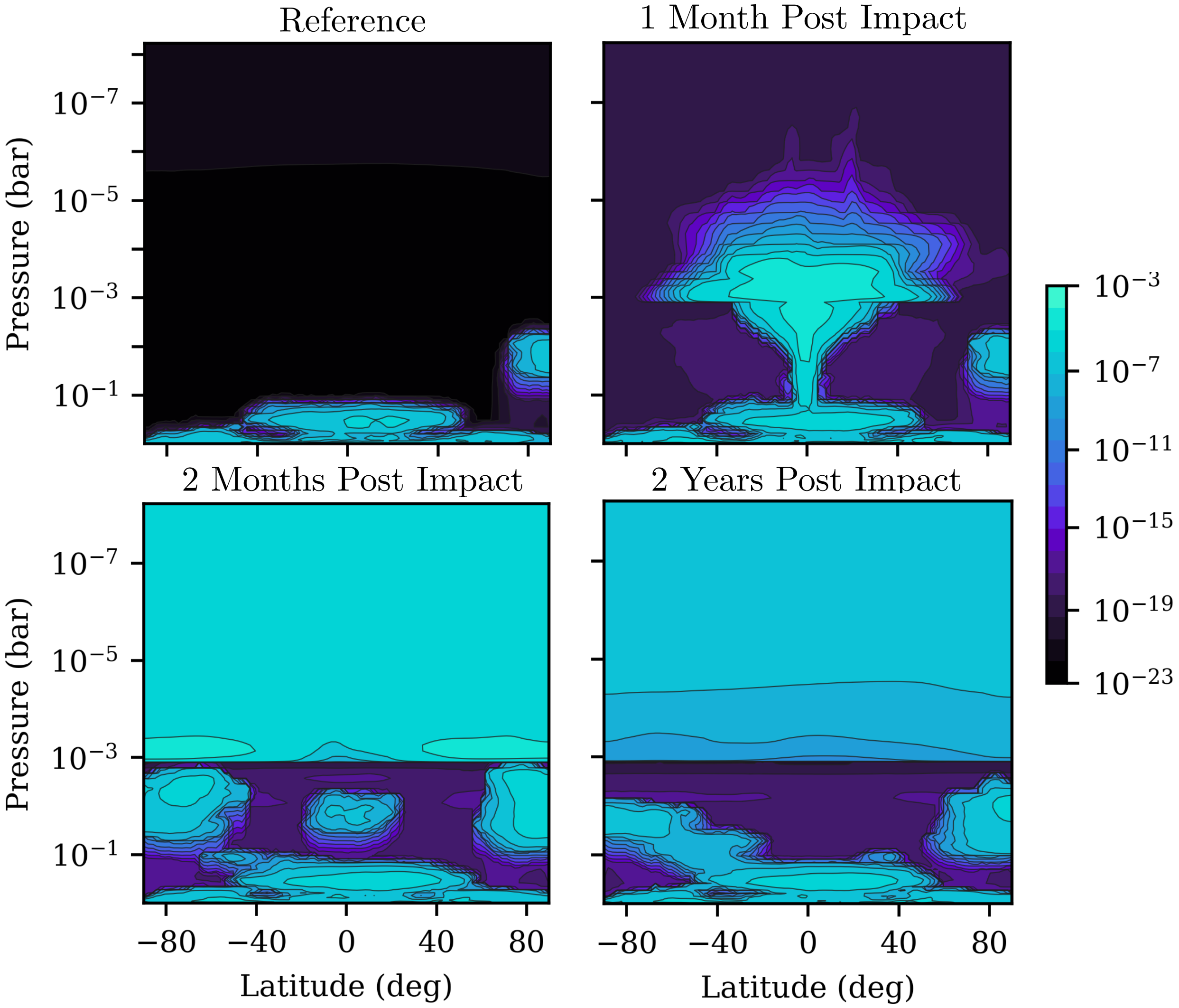

Figure 12. Zonally and temporally averaged cloud ice mixing ratio for our reference nonimpacted model (top left) and at three points in time for our fiducial model: 1 month (top right), 2 months (bottom left), and 2 yr (bottom right) postimpact, with the latter times selected to correspond to the spectra shown in Figure 11.

albeit to a lesser extent as many of these molecules exhibit enhanced low-pressure abundances as opposed to the reduction found for ozone (see Section 3.3). Note that, at this point in time postimpact, impact-driven changes in the strength of spectroscopic features are relatively slow to evolve and hence should remain observable when combining transit observations taken over a period of weeks to months (as is typically done for habitable-zone planets around M dwarfs), assuming that activity from the host M-star does not wash out the features entirely (see the discussion of this problem by, for example, R. Doyon 2024).

Finally, 2 yr postimpact we find a transmission spectrum that is extremely similar to our nonimpacted reference state, albeit with some slight differences in feature strength, particularly ozone, although other oxygen-rich molecules also show slight changes, such as an enhancement in the strength of CO_2 features. Unfortunately most if not all of these differences are unlikely to be distinguishable observationally given that, even when we combine multiple transits, they fall below the noise floor of JWST (see, for example, the noise estimates of Z. Rustamkulov et al. 2022).

The effects of a single icy cometary impact on the thermal emission spectrum, which we show on the bottom row of Figure 11, are more muted. Primarily this is because cloud ice scattering does not have the same effect on planetary emission as it does on a transmission spectrum. As such, at most of the wavelengths considered here, we find spectral feature differences that are far below the noise floor of JWST or other upcoming space-based telescopes. The only exception to this is between ∼14 and ∼16 μm, where we find a water-opacity-driven change in the CO_2 feature. Specifically, we find that the increased opacity of the atmosphere masks CO_2 absorption features, leading to an emission spectrum that is closer to a blackbody. When comparing this region with our nonimpacted reference state, we find a ∼25 ppm enhancement 2 months postimpact, and the change remains potentially observable for up to 1 yr postimpact (with a ∼15 ppm enhancement). Note that a similar, but much weaker and hence likely unobservable, effect is found for the ozone feature at ∼9.8 μm, where we again find a slight (a few ppm) increase in thermal emission contrast postimpact. Here, however, the difference is not driven by water opacity masking the ozone feature, but instead it is due to a decrease in ozone abundance. This reinforces the need to take care when interpreting emission and transmission spectra due to the complex and wavelength-dependent relationships between observed abundances and the strength of atmospheric features.

Given all of the above, as well as an understanding of current and near-future observational capabilities, we suggest that individual cometary impacts are likely to be detectable only for a short period postimpact. In the transmission spectrum, this will be driven by the effects of cloud ice scattering at low pressures, leading to a substantial and measurable increase and decrease in apparent planetary radius and spectroscopic feature strength, respectively. Atmospheric water plays a similar role on the emission spectra, masking atmospheric features in a way that may be observable for a short while postimpact.

One way this might manifest is as a difference between repeated observations of the same object, an effect that might indicate that a cometary impact has changed the observed atmospheric chemistry/composition for one (or more) of our observations. As the number of atmospheres characterized increases, and we take repeat observations of these atmospheres in order to further probe their composition, the chances that such a scenario will occur increase.

Beyond the short-lived effects associated with a cometary impact, repeated impacts or ongoing bombardment have the potential to deliver enough material to drive a global change in atmospheric chemistry, composition, and climate (as might have been the case for the early Earth).

4. Concluding Remarks

In this work we have coupled the cometary impact model of F. Sainsbury-Martinez & C. Walsh (2024), which includes thermal ablation at low pressures and breakup deeper with the atmosphere, with the Earth system model WACCM6/CESM2. This coupled model was then used to simulate the impact of a pure water ice comet (with $R = 2.5$ km and $\rho = 1\ \mathrm{g\,cm^{-3}}$) with the dayside (substellar point) of a tidally locked, terrestrial exoplanet modeled on the potentially habitable exoplanet TRAPPIST-1e. Our fiducial model included both the mass (water) and thermal energy deposition associated with the cometary impact, and we compared our results with a nonimpacted reference state.

Our analysis of this fiducial coupled model, as well as two additional models (see the Appendix) that isolated the effects of cometary water and thermal energy delivery, allowed us to investigate the strength and timescale of the atmosphere's response to each component of the impact and revealed the significant role that water delivery can play in modifying our exoplanetary atmosphere. The main takeaway results of our study are as follows:

1. While the majority of the cometary water/ice is deposited at pressures $>10^{-5}$ bar, vertical advection then rapidly carries this water aloft, enriching the atmosphere for all pressures, including a multi-order-of-magnitude enhancement in the outer atmosphere.
2. This enhancement in mid- and outer-atmosphere water persists for at least 10 yr postimpact.
3. The impact of the cometary heating is more limited: it increases the fractional water abundance at higher pressures by evaporating/sublimating atmospheric water droplets (e.g., rain/snow) and ice particles.
4. Deposited water acts as a strong opacity source, driving localized dayside heating (an increase of up to 35 K) that peaks in strength at $\sim 5 \times 10^{-4}$ bar. In turn, this enhanced midatmosphere opacity reduces the surface insolation, reducing the (near-)surface temperature by up to 2 K.
5. The deposited water, due to its high UV opacity, rapidly photodissociates, increasing the abundance of hydrogen and hydroxyl radicals (OH) by up to $\sim$3 orders of magnitude.
6. The formation and further photodissociation of hydrogen and hydroxyl radicals (OH) lead to an increase in the hydrogen and oxygen content of the atmosphere and the formation of, for example, H_2, O_2, CH_4, N_2O, NO, NO_2, NO_3, and HO_2.
7. Despite the increase in atmospheric oxygen, the formation of NO_x and HO_x results in significant ozone (O_3) destruction. For example, the column-integrated ozone content drops by $\sim$7.5% for the first 5 yr postimpact.
8. Zonal winds, driven by the tidally locked insolation, rapidly homogenize the deposited water zonally, suggesting that similar results to those found here should apply for any equatorial impact.
9. Horizontal winds also influence the water photolysis rate, enhancing it at early times by increasing the surface area of enriched water interacting with UV irradiation and decreasing it at later times by advecting water to the dark nightside. Such an effect can only be captured when considering the full 3D atmospheric circulation.
10. The deposited water drives the formation of high-latitude clouds and high-altitude cloud ice. Scattering by this cloud ice significantly affects the transmission spectra postimpact, increasing the apparent near-infrared atmospheric thickness from $\sim$14 to $>$38 km 2 months postimpact, reducing to a $\sim$5 km enhancement 1 yr postimpact.
11. The impact-induced changes in atmospheric composition also affect the strength of absorption and emission features in the transmission and emission spectra. For example, we find a decrease in the strength of ozone absorption and emission features and an increase in the strength of water absorption features. We also find that the increased opacity of the atmosphere masks deep CO_2 features in the postimpact emission spectrum.

The aforementioned results vis-à-vis the transmission and thermal emission spectra suggest that the effects of a cometary impact should be most visible within 1 yr of the impact, with the strong-cloud ice-driven changes to the transmission spectrum being potentially detectable from a single transit observation. However, as the atmosphere settles back toward the nonimpacted reference state, we find that the long-lasting changes associated with a single cometary impact fall below the noise floor of modern near-infrared telescopes, making them unlikely to be observed. As such, the most-likely scenario under which a single large impact will be observed is a short-lived (i.e., single-observation) change in the spectra of a planet that has undergone repeated observations. However, we acknowledge that such an event is rather unlikely for a terrestrial planet with a potentially habitable secondary atmosphere. For example, D. W. Hughes (2000) calculates that the time interval between impacts that lead to significant $>$2 km diameter craters should be more than 190,000 yr. On the other hand, given the massive numbers of planets that have been and soon will be detected, we also expect that ongoing monitoring of these objects may be able to reveal such an event.

Instead, the fact that impact-driven changes in atmospheric chemistry and composition persist to quasi–steady state suggests another scenario. It is possible that repeated or ongoing bombardment might drive large-scale and long-term changes, which might even play a role in shaping planetary habitability. This is particularly true for young planets, where we expect the bombardment rate to be significantly higher (as was the case for the Earth; e.g., C. I. Fassett & D. A. Minton 2013; G. R. Osinski et al. 2020), and for which icy comets may play an important role in delivering volatile materials (see, for example, T. Owen & A. Bar-Nun 1995; P. Ehrenfreund et al. 2002; M. Y. Marov & S. I. Ipatov 2018, 2023). We will explore this in a future study, using our coupled impact/climate model to study the effects of repeated cometary bombardment for both oxygen-rich and oxygen-poor nitrogen-dominated atmospheres. However, in the next paper in this series we will compare the results from this study to a model of an icy cometary impact with a true exo-Earth-analog planet that includes a diurnal cycle and hence rather different atmospheric circulations and water insolation patterns (Paper II).

Acknowledgments

The authors would like to thanks Richard Anslow for pointing out the error in Equation (3). F.S.-M. and C.W. would like to thank UK Research and Innovation for support under grant No. MR/T040726/1. Additionally, C.W. would like to thank the University of Leeds and the Science and Technology Facilities Council for their financial support (ST/X001016/1). This work was undertaken on ARC4, part of the high-performance computing facilities at the University of Leeds, UK.

Appendix
Results: Isolated Deposition

To better isolate how different components of the icy cometary impact influence the atmospheres of our tidally locked, terrestrial exoplanetary atmosphere, we also ran a pair of models in which we isolated/disentangled the effects of mass/water (red) and thermal energy (green/blue) deposition (Figure 1). As was the case in our fiducial model, we consider the impact of a pure water ice comet with a radius of 2.5 km and a density of 1 g cm^{-3} (Table 1) and evolve the model for 20 yr, within which time both models approach a quasi–steady state in which the scale of the oscillations in the global mean temperature and fractional water abundance are similar to that found in our reference nonimpacted atmosphere. By isolating the deposition in this way we can study the timescale and strength of the atmosphere's response to both components of the cometary material delivery independently, using this knowledge to better interpret our fiducial model that introduced both deposition profiles to our atmospheric model simultaneously (Section 3).

A.1. Isolated Water Deposition

We start by exploring the isolated effects of cometary water delivery on our tidally locked Earth-like atmosphere. For this isolated water deposition scenario, Figure 13 shows how the fractional water abundance (top row) and mean temperature (bottom) vary both shortly after impact (left column) and over the ~20 yr required for the model atmosphere to reach a quasi–steady state (right column). As in our fiducial case (Section 3.1), we find that while most of the water is delivered to pressures $>10^{-4}$ bar, vertical transport rapidly carries this water aloft, where it persists as a multi-order-of-magnitude enhancement for at least 5 yr postimpact. However, as shown in Figure 14, the enhancement in both the midatmosphere (top middle) and outer-atmosphere (top left) water abundance (blue) is weaker and very slightly shorter-lived than in our fiducial model (green), the latter of which combines the effects of both water/mass and thermal energy deposition. As we discuss below (Appendix A.2), the underlying cause of this is the thermal energy from the cometary impact driving water/ice evaporation/sublimation, particularly in the midatmosphere.

In turn, as was found for our fiducial model, this impact-enhanced midatmosphere water vapor acts as a strong source of opacity, absorbing incoming radiation and driving local heating. However, the lower peak fractional water abundance when compared with our fiducial model in turn drives a weaker local heating effect: at its peak in the resolved, i.e., non-time-averaged, data we find a midatmosphere temperature inversion that is ~35 K hotter than the same location in our nonimpacted reference case (shown in gray). This is ~5 K cooler than the same peak found in our fiducial, combined deposition case. A similar story holds true for the average midatmosphere temperature, which is ~10 K hotter than our nonimpacted reference state while also, again, being ~5 K cooler than our fiducial model.

Differences between the isolated water deposition and fiducial models are also apparent in the deep atmosphere. As seen in the top-right panel of Figure 14, our isolated water deposition profile exhibits a slightly stronger postimpact water enhancement than our fiducial case. The underlying driver of this is a slight cooling of the deep atmosphere (bottom-right panel of Figure 14), driven by the absorption of incoming irradiation in the midatmosphere (which is stronger in our fiducial case due to the enhanced water vapor content), which leads to enhanced formation of snow/ice.

Overall, we find that while the changes driven by the isolated delivery of cometary water are similar to those seen in our fiducial model, differences are also abundantly clear. To better understand these differences, we also explored the isolated effects of impact-driven thermal energy deposition on our tidally locked Earth-like atmosphere.

A.2. Isolated Thermal Energy Deposition

As might be expected due to differences in typical radiative (weeks to months) and dynamical (i.e., chemical mixing/transport—months to years) timescales, the atmospheric response to the thermal energy deposition is much shorter-lived than the changes associated with cometary water. This can be seen in both Figure 15, which shows how the fractional water abundance (top row) and mean temperature (bottom) vary both in the very first days postimpact (left) and over the <1 yr required for radiative effects to fully dissipate (right column), and the purple time evolution curves of Figure 14.

For example, the slight temperature enhancement in the midatmosphere, where most of the kinetic energy is deposited due to the cometary breakup, almost completely dissipates within 1 month of the impact. The remainder, <1 K with respect to our nonimpacted reference state, dissipates over the following months.

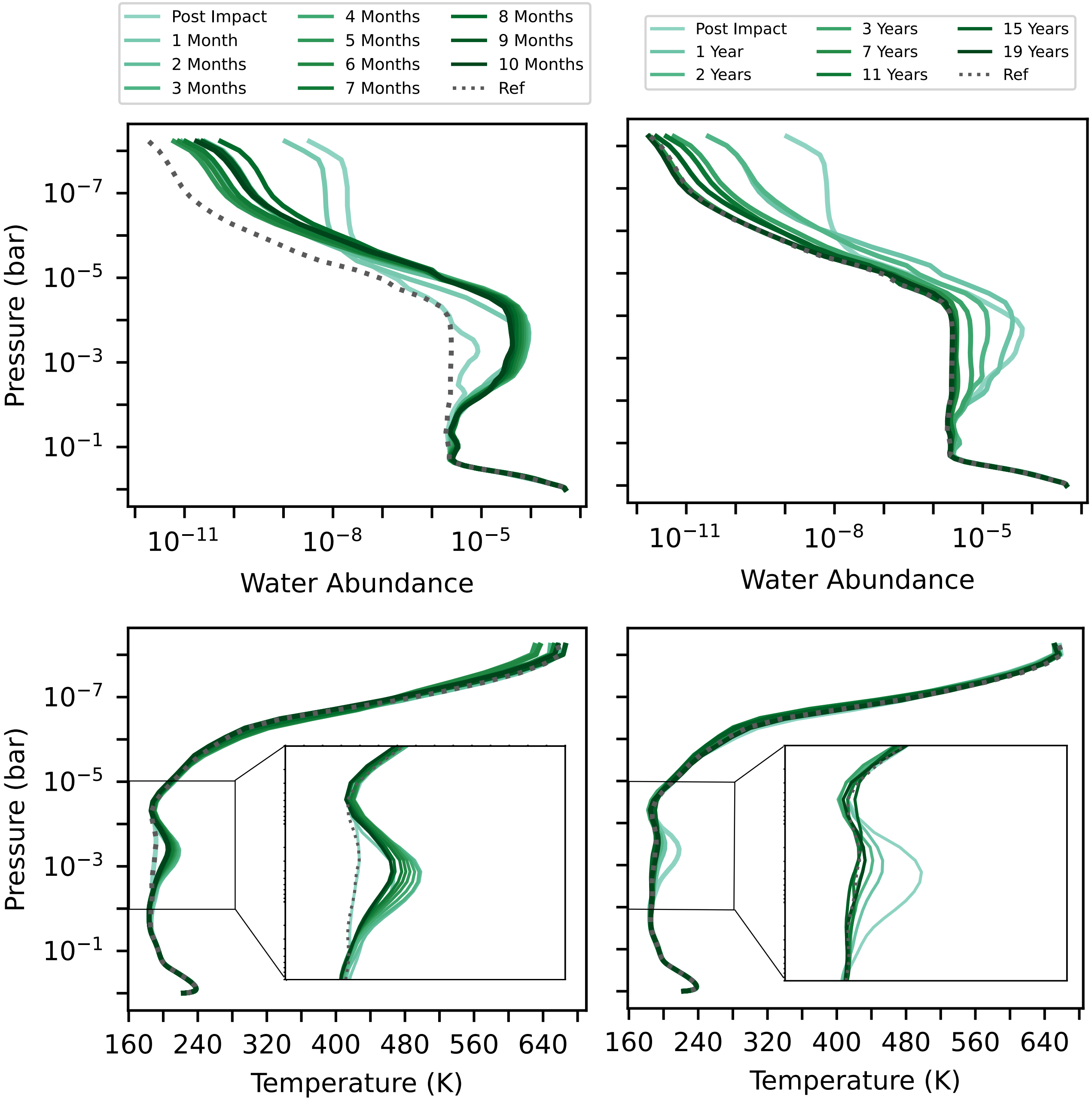

Figure 13. Fractional water abundance (top) and temperature (bottom) profiles showing the rapid atmospheric evolution within the first 10 months (left) of the isolated deposition of water from an icy cometary impact and the slower but steady settling of the atmosphere into a quasi–steady state (right) reminiscent of the nonimpacted reference state (gray dashed). Here each profile is calculated by averaging both horizontally over all latitudes and longitudes and temporally over 1 month of simulation time. To better demonstrate the change in temperature in the midatmosphere, we include an inset showing a zoomed-in view of the temperature profile between 10^{-2} and 10^{-5} bar.

A similar story holds true in both the outer and deep atmosphere; however, in both of these regions we also find that the heating has a knock-on effect on the atmospheric composition: a slight increase in the fractional water abundance relative to our nonimpacted reference state. This occurs because the thermal energy from the cometary impact causes some of the frozen (ice/snow) and liquid (rain) water to sublimate/evaporate, leading to a weak local enhancement in the fractional water abundance, particularly near the surface (see the top-right panel of Figure 14). While these changes to the water vapor content of the atmosphere are small relative to those associated with the cometary mass (water) deposition, our fiducial model reveals how the inclusion of thermal energy deposition in a combined deposition model results in a distinct climate from that found when considering water deposition alone.

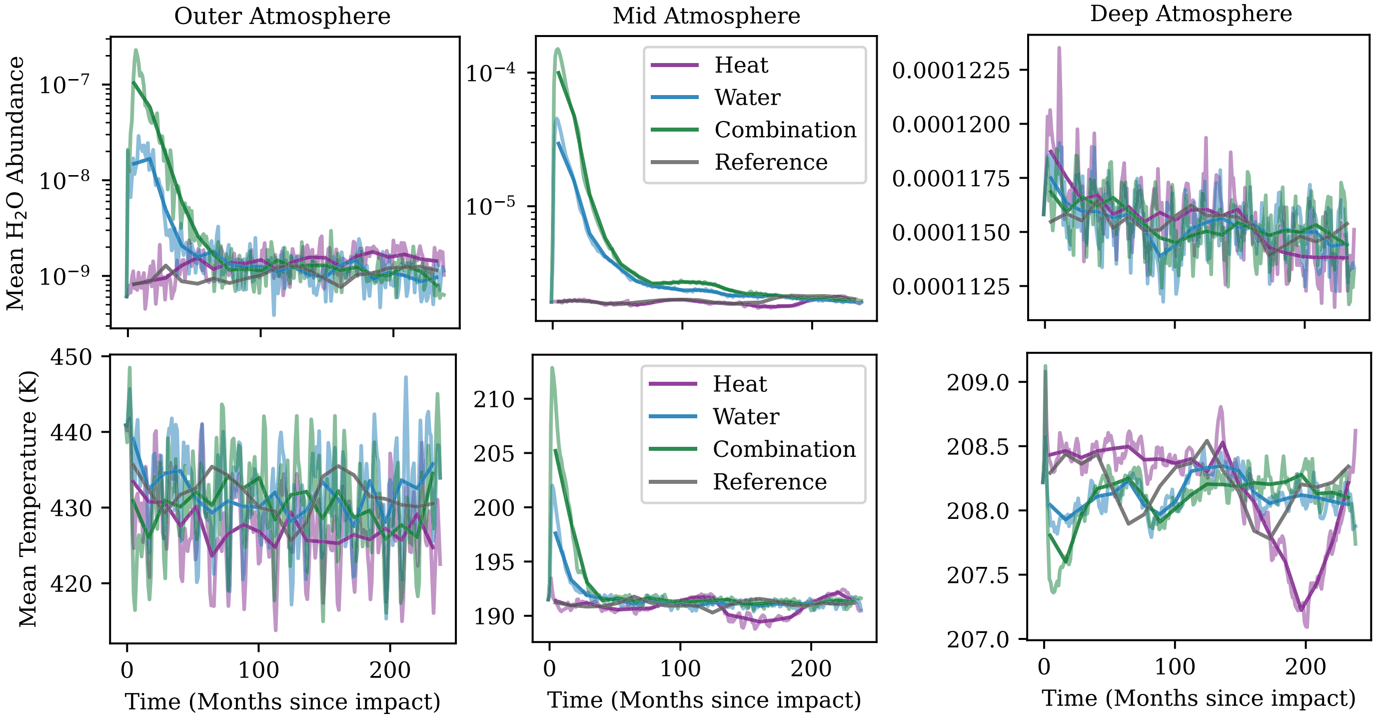

Figure 14. Time evolution of the annual mean (solid lines) and monthly mean (faint lines) fractional water abundance (top row) and temperature (bottom) in the outer atmosphere ($P < 10^{-5}$ bar; left), midatmosphere ($10^{-5} > P > 10^{-2}$ bar; middle), and near the surface ($P > 10^{-2}$ bar; right) for all four models considered here: our water deposition–only model (blue), thermal energy deposition–only model (purple), fiducial model (i.e., combined water and thermal deposition; green), and nonimpacted reference state (gray).

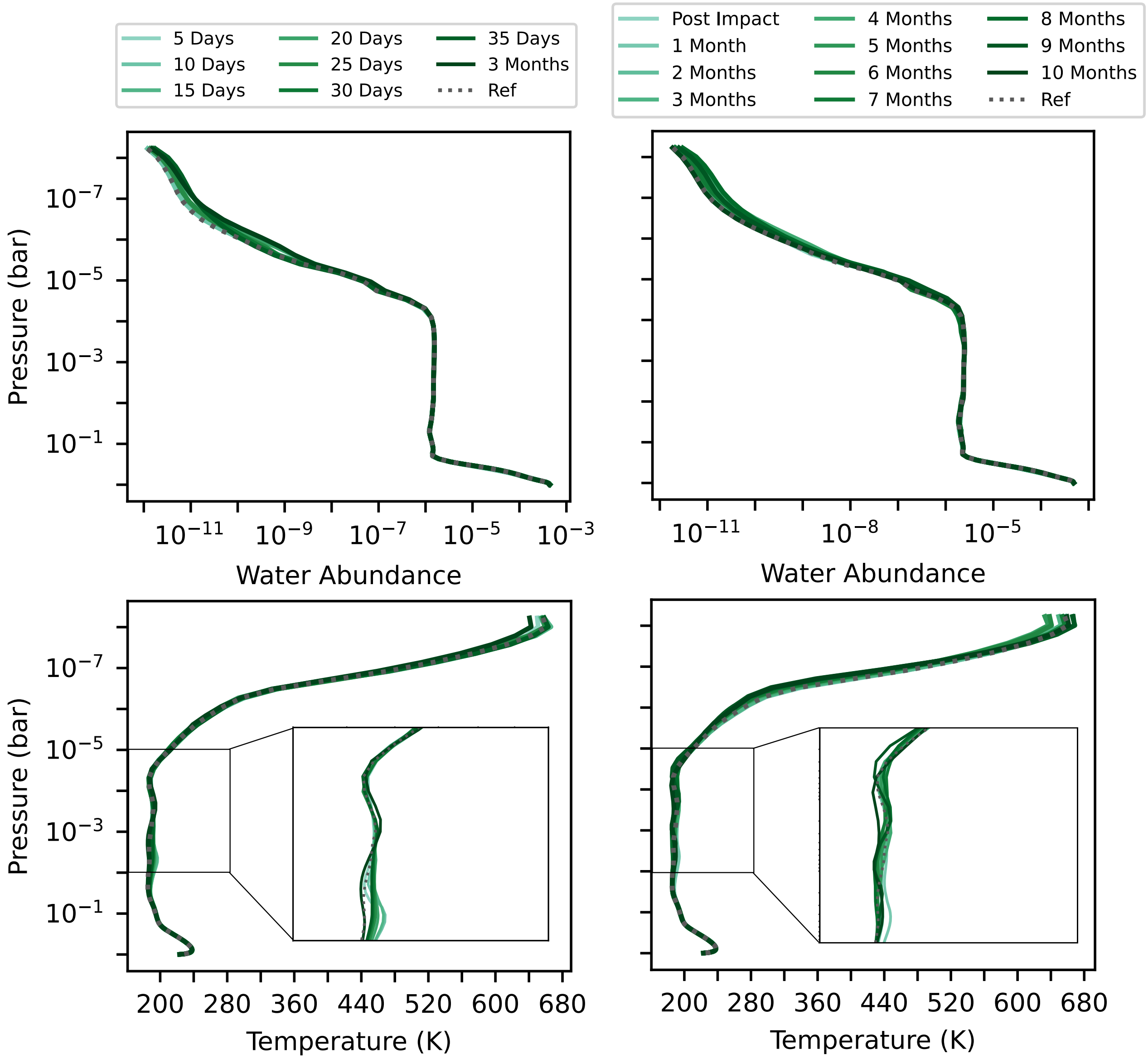

Figure 15. Fractional water abundance (top) and temperature (bottom) profiles showing the limited long-term effects of the isolated heat deposition from the impact of a pure water ice comet. Here we plot the horizontally averaged—over all latitudes and longitudes—profiles within the first 3 months (taken from 5 day means; left) and the first 10 months (taken from monthly means; right) of the impact and compare them to our nonimpacted reference state (gray dashed). To better demonstrate the change in temperature in the midatmosphere, we include an inset showing a zoomed-in view of the temperature profile between 10^{-2} and 10^{-5} bar. Note the difference in timescale when compared with our water deposition and combined deposition simulations.

ORCID iDs

F. Sainsbury-Martinez https://orcid.org/0000-0003-0304-7931
C. Walsh https://orcid.org/0000-0001-6078-786X

References

Agol, E., Dorn, C., Grimm, S. L., et al. 2021, PSJ, 2, 1
A'Hearn, M. F. 2011, ARA&A, 49, 281
Alibert, Y., & Benz, W. 2017, A&A, 598, L5
Alibert, Y., Mordasini, C., Benz, W., & Winisdoerffer, C. 2005a, A&A, 434, 343
Alibert, Y., Mousis, O., Mordasini, C., & Benz, W. 2005b, ApJL, 626, L57
Anslow, R. J., Bonsor, A., & Rimmer, P. B. 2023, RSPSA, 479, 20230434
Barnes, R. 2017, CeMDA, 129, 509
Benz, W., Slattery, W. L., & Cameron, A. G. W. 1988, Icar, 74, 516
Bhongade, A., Marsh, D. R., Sainsbury–Martinez, F., & Cooke, G. 2024, ApJ, 977, 9696
Bottke, W. F., & Norman, M. D. 2017, AREPS, 45, 619
Braam, M., Palmer, P. I., Decin, L., Cohen, M., & Mayne, N. J. 2023, MNRAS, 526, 263
Brasser, R., Werner, S. C., & Mojzsis, S. J. 2020, Icar, 338, 113514
Burrows, A., Rauscher, E., Spiegel, D. S., & Menou, K. 2010, ApJ, 719, 341
Carone, L., Keppens, R., & Decin, L. 2015, MNRAS, 453, 2412
Chen, H., Wolf, E. T., Kopparapu, R., Domagal-Goldman, S., & Horton, D. E. 2018, ApJL, 868, L6
Childs, A. C., Martin, R. G., & Livio, M. 2022, ApJL, 937, L41
Chyba, C. F., Thomas, P. J., Brookshaw, L., & Sagan, C. 1990, Sci, 249, 366
Cooke, G. J., Marsh, D. R., Walsh, C., Rugheimer, S., & Villanueva, G. L. 2022, MNRAS, 518, 206
Cooke, G. J., Marsh, D. R., Walsh, C., & Youngblood, A. 2023, ApJ, 959, 45
Cooke, G. J., Marsh, D. R., Walsh, C., & Sainsbury–Martinez, F. 2024, PSJ, 5, 168
Delrez, L., Gillon, M., Triaud, A. H. M. J., et al. 2018, MNRAS, 475, 3577
Delsemme, A. H. 2000, Icar, 146, 313
Dole, S. H. 1964, Habitable Planets for Man (New York: Blaisdell)
Doyon, R. 2024, arXiv:2403.12617

Ehrenfreund, P., Irvine, W., Becker, L., et al. 2002, in ESA Special Publication 518, Proc.of the First European Workshop on Exo-Astrobiology, ed. H. Lacoste (Noordwijk: ESA), 9

Emmons, L. K., Schwantes, R. H., Orlando, J. J., et al. 2020, JAMES, 12, e2019MS001882

Fassett, C. I., & Minton, D. A. 2013, NatGe, 6, 520

Fauchez, T. J., Turbet, M., Sergeev, D. E., et al. 2021, PSJ, 2, 106

Fauchez, T. J., Villanueva, G. L., Sergeev, D. E., et al. 2022, PSJ, 3, 213

Field, G. B., & Ferrara, A. 1995, ApJ, 438, 957

Fortney, J. J., Lodders, K., Marley, M. S., & Freedman, R. S. 2008, ApJ, 678, 1419

Fortney, J. J., & Nettelmann, N. 2010, SSRv, 152, 423

Frantseva, K., Mueller, M., Pokorný, P., van der Tak, F. F. S., & ten Kate, I. L. 2020, A&A, 638, A50

Gettelman, A., Mills, M. J., Kinnison, D. E., et al. 2019, JGRD, 124, 12380

Gillon, M., Jehin, E., Fumel, A., et al. 2013, in EPJ Web of Conf., Vol. 47, Hot Planets and Cool Stars (Garching: EDP Sciences), 03001

Gillon, M., Jehin, E., Lederer, S. M., et al. 2016, Natur, 533, 221

Grenfell, J. L., Gebauer, S., Paris, v., Godolt, M., & Rauer, H. 2014, P&SS, 98, 66

Grimm, S. L., Demory, B.-O., Gillon, M., et al. 2018, A&A, 613, A68

Guillot, T., Stevenson, D. J., Hubbard, W. B., & Saumon, D. 2004, in Jupiter. The Planet, Satellites and Magnetosphere, Vol. 1, ed. F. Bagenal, T. E. Dowling, & W. B. McKinnon (Cambridge: Cambridge Univ. Press), 35

Hughes, D. W. 2000, MNRAS, 317, 429

Ipatov, S. I., & Mather, J. C. 2003, EM&P, 92, 89

Ipatov, S. I., & Mather, J. C. 2004, AdSpR, 33, 1524

Itcovitz, J. P., Rae, A. S. P., Citron, R. I., et al. 2022, PSJ, 3, 115

Kopparapu, R. K., Ramirez, R., Kasting, J. F., et al. 2013, ApJ, 765, 131

Korycansky, D. G., Zahnle, K. J., & Low, M.-M. M. 2002, Icar, 157, 1

Kozakis, T., Mendonça, J. M., & Buchhave, L. A. 2022, A&A, 665, A156

Lin, J., & Qian, T. 2022, AtO, 60, 1

Liu, B., Marsh, D. R., Walsh, C., & Cooke, G. 2023, MNRAS, 524, 1491

Mac Low, M.-M., & Zahnle, K. 1994, ApJL, 434, L33

Marov, M. Y., & Ipatov, S. I. 2005, SoSyR, 39, 374

Marov, M. Y., & Ipatov, S. I. 2018, SoSyR, 52, 392

Marov, M. Y., & Ipatov, S. I. 2023, PhyU, 66, 2

Meadows, V. S., Reinhard, C. T., Arney, G. N., et al. 2018, AsBio, 18, 630

Mordasini, C., van Boekel, R., Mollière, P., Henning, T., & Benneke, B. 2016, ApJ, 832, 41

Müller, S., & Helled, R. 2024, ApJ, 967, 7

Nesvorný, D., Dones, L., De Prá, M., Womack, M., & Zahnle, K. J. 2023, PSJ, 4, 139

O'Brien, D. P., Walsh, K. J., Morbidelli, A., Raymond, S. N., & Mandell, A. M. 2014, Icar, 239, 74

Osinski, G. R., Cockell, C. S., Pontefract, A., & Sapers, H. M. 2020, AsBio, 20, 1121

Owen, T., & Bar-Nun, A. 1995, Icar, 116, 215

Passey, Q. R., & Melosh, H. J. 1980, Icar, 42, 211

Peacock, S., Barman, T., Shkolnik, E. L., Hauschildt, P. H., & Baron, E. 2019, ApJ, 871, 235

Pokorný, P., Sarantos, M., & Janches, D. 2017, ApJL, 842, L17

Proedrou, E., & Hocke, K. 2016, EP&S, 68, 96

Rustamkulov, Z., Sing, D. K., Liu, R., & Wang, A. 2022, ApJL, 928, L7

Sainsbury-Martinez, F., & Walsh, C. 2024, ApJ, 966, 39

Sainsbury-Martinez, F., Walsh, C., Cooke, G. J., & Marsh, D. R. 2024, ApJ, 974, 139

Seager, S., & Sasselov, D. D. 2000, ApJ, 537, 916

Sergeev, D. E., Fauchez, T. J., Turbet, M., et al. 2022, PSJ, 3, 212

Showman, A. P., & Polvani, L. M. 2011, ApJ, 738, 71

Showman, A. P., Wordsworth, R. D., Merlis, T. M., & Kaspi, Y. 2013, in Comparative Climatology of Terrestrial Planets, ed. S. J. Mackwell et al. (Tucson, AZ: Univ. Arizona Press), 277

Smallwood, J. L., Martin, R. G., Lepp, S., & Livio, M. 2018, MNRAS, 473, 295

Staguhn, J., Mandell, A, Stevenson, K., et al. 2019, BAAS, 51, 238

Svetsov, V. V., Nemtchinov, I. V., & Teterev, A. V. 1995, Icar, 116, 131

Todd, Z. R., & Öberg, K. I. 2020, AsBio, 20, 1109

Turbet, M., Fauchez, T. J., Sergeev, D. E., et al. 2022, PSJ, 3, 211

Valle, G., Dell'Omodarme, M., Prada Moroni, P. G., & Degl'Innocenti, S. 2014, A&A, 567, A133

Villanueva, G. L., Smith, M. D., Protopapa, S., Faggi, S., & Mandell, A. M. 2018, JQSRT, 217, 86

Wennberg, P. O., Cohen, R. C., Stimpfle, R. M., et al. 1994, Sci, 266, 398

Wolf, E. T. 2017, ApJL, 839, L1

Woo, J. M. Y., Genda, H., Brasser, R., & Mojzsis, S. J. 2019, Icar, 333, 87

Yates, J. S., Palmer, P. I., Manners, J., et al. 2020, MNRAS, 492, 1691